

AD-A167 270

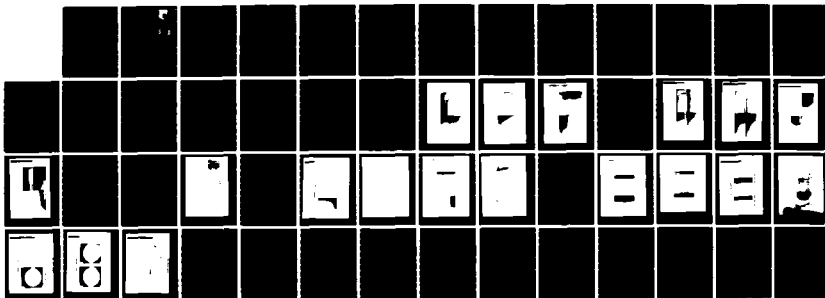
A NEW RADIOGRAPHIC CORROSION INSPECTION CAPABILITY(U)
ADVANCED RESEARCH AND APPLICATIONS CORP SUNNYVALE CA
J H STANLEY ET AL. JAN 86 FR85-352-1 AFMAL-TR-85-4130
F33615-84-C-5089

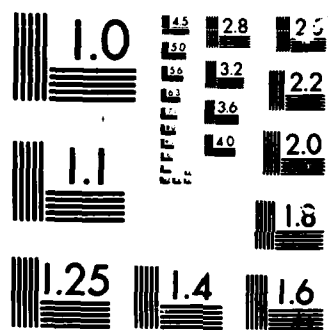
1/1

UNCLASSIFIED

F/G 14/5

NL





MICROCOPY

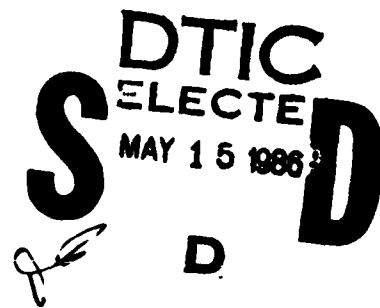
CHART



AFWAL TR-85-4130

A NEW RADIOGRAPHIC CORROSION INSPECTION CAPABILITY

J. H. STANLEY
J. J. LEPAGE



ADVANCED RESEARCH AND APPLICATIONS CORPORATION
1223 EAST ARQUES AVENUE
SUNNYVALE, CALIFORNIA 94086

JANUARY 1986

Final Report: 2 JULY 1984 - 2 JANUARY 1985

APPROVED FOR PUBLIC RELEASE; DISTRIBUTION UNLIMITED

MATERIALS LABORATORY
AIR FORCE WRIGHT AERONAUTICAL LABORATORIES
AIR FORCE SYSTEM COMMAND
WRIGHT-PATTERSON AIR FORCE BASE, OHIO 45433-6533

DTIC COPY

86 5 15 00 4


AD-A167 270

NOTICE

When Government drawings, specifications, or other data are used for any purpose other than in connection with a definitely related Government procurement operation, the United States Government thereby incurs no responsibility nor any obligation whatsoever; and the fact that the government may have formulated, furnished, or in any way supplied the said drawings, specifications, or other data, is not to be regarded by implication or otherwise as in any manner licensing the holder or any other person or corporation, or conveying any rights or permission to manufacture use, or sell any patented invention that may in any way be related thereto.

This report has been reviewed by the Office of Public Affairs (ASD/PA) and is releasable to the National Technical Information Service (NTIS). At NTIS, it will be available to the general public, including foreign nations.

This technical report has been reviewed and is approved for publication.


JAMES A. HOLLOWAY
Project Engineer
Non-Destructive Evaluation Branch

FOR THE COMMANDER


DONALD M. FORNEY
Chief, Non-Destructive Evaluation Branch
Metals & Ceramics Division

"If your address has changed, if you wish to be removed from our mailing list, or if the addressee is no longer employed by your organization please notify AFWAL/MLLP, W-PAFB, OH 45433 to help us maintain a current mailing list".

Copies of this report should not be returned unless return is required by security considerations, contractual obligations, or notice on a specific document.

Unclassified

SECURITY CLASSIFICATION OF THIS PAGE

REPORT DOCUMENTATION PAGE

1a. REPORT SECURITY CLASSIFICATION Unclassified			1b. RESTRICTIVE MARKINGS	
2a. SECURITY CLASSIFICATION AUTHORITY			3. DISTRIBUTION / AVAILABILITY OF REPORT Approved for public release; distribution unlimited.	
2b. DECLASSIFICATION / DOWNGRADING SCHEDULE				
4. PERFORMING ORGANIZATION REPORT NUMBER(S) FR85-352-1			5. MONITORING ORGANIZATION REPORT NUMBER(S) AFWAL-TR-85-4130	
5a. NAME OF PERFORMING ORGANIZATION Advanced Research and Applications Corp.		6b. OFFICE SYMBOL (If applicable) 7N082	7a. NAME OF MONITORING ORGANIZATION Materials Laboratory (AFWAL/MLLP) A. F. Wright Aeronautical Labs	
6c. ADDRESS (City, State, and ZIP Code) 1223 E. Arques Ave. Sunnyvale, CA 94086			7b. ADDRESS (City, State, and ZIP Code) Wright-Patterson AFB, OH 45433	
8a. NAME OF FUNDING / SPONSORING ORGANIZATION DCASR - Los Angeles		8b. OFFICE SYMBOL (If applicable) S0506A	9. PROCUREMENT INSTRUMENT IDENTIFICATION NUMBER F33615-84-C-5089	
9c. ADDRESS (City, State, and ZIP Code) P. O. Box 45011 Los Angeles, CA 90045			10. SOURCE OF FUNDING NUMBERS	
			PROGRAM ELEMENT NO.	PROJECT NO.
			TASK NO.	WORK UNIT ACCESSION NO.
11. TITLE (Include Security Classification) A New Radiographic Corrosion Inspection Capability				
12. PERSONAL AUTHOR(S) J. H. Stanley and J. J. LePage				
13a. TYPE OF REPORT Final		13b. TIME COVERED FROM 7/2/84 TO 1/2/85		14. DATE OF REPORT (Year, Month, Day) January 1986
15. PAGE COUNT 42				
16. SUPPLEMENTARY NOTATION				
17. COSATI CODES			18. SUBJECT TERMS (Continue on reverse if necessary and identify by block number)	
FIELD	GROUP	SUB-GROUP		
			dual energy photoelectric	
			digital radiography corrosion	
			Compton non-destructive evaluation	
19. ABSTRACT (Continue on reverse if necessary and identify by block number) A dual-energy radiographic technique is reported which could significantly enhance the corrosion detection and damage assessment capabilities of any radiometric system. Digital radiographs taken at two different effective energies are manipulated in such a way as to greatly improve the conspicuity of detail in the image by reducing the amount of structural noise present. The improved sensitivity offered by the method can be traded for an equivalent detectability at a much lower dose level, an important consideration for on-board or in-situ inspections. In addition, the technique allows the user to identify materials in the object under examination, an important consideration when foreign material is present. Results indicate that the effective atomic number of unknown contaminants can be determined to better than 3% absolute error.				
20. DISTRIBUTION / AVAILABILITY OF ABSTRACT <input type="checkbox"/> UNCLASSIFIED/UNLIMITED <input checked="" type="checkbox"/> SAME AS RPT. <input type="checkbox"/> DTIC USERS			21. ABSTRACT SECURITY CLASSIFICATION Unclassified	
22a. NAME OF RESPONSIBLE INDIVIDUAL James Holloway			22b. TELEPHONE (Include Area Code) 513/255-5309	22c. OFFICE SYMBOL AFWAL/MLLP

SUMMARY

Corrosion of equipment and material is an ubiquitous national problem costing the U.S. economy over \$70 billion annually. Real-time radiography has been identified as one of several promising new NDE technologies because of its potential ability to solve a significant number of existing corrosion inspection problems. Yet, in spite of its potential advantages, real-time radiography has not yet demonstrated a significantly better ability than other competing modalities to detect the early stages of corrosion when corrective actions can most efficiently be taken. A dual-energy radiographic technique is reported which will significantly enhance the corrosion detection and damage assessment capabilities of any radiometric system. The main advantage of the proposed method is that it improves the conspicuity of detail in a digital radiograph by greatly reducing the structural noise in the image. The improved sensitivity offered by dual-energy methods can be traded for an equivalent detectability at a much lower dose level, an important consideration for on-board or in-situ inspections. In addition, dual-energy radiography also allows the user to identify materials in the object under examination, an important consideration when foreign material is present. Results presented here indicate that the effective atomic number can be determined to better than 3% absolute error.

This newly developed dual-energy technique impacts many areas of corrosion inspection and diagnosis. In those areas where real-time radiography has already demonstrated, or is expected to demonstrate, an ability to produce useful inspections, the technique will serve to improve the sensitivity of the examination and perhaps expand the range of valid applications. In those inspection areas where real-time radiography offers at best a marginal detection capability, dual-energy processing may make some otherwise impractical applications feasible. Although the initial application is expected to be in the detection and assessment of corrosion, the dual-energy method is considerably more powerful and more general in nature and could rapidly become a standard radiographic procedure.

PREFACE

This is the final report for work performed by Advanced Research and Applications Corporation (ARACOR) under AFWAL Contract Number F33615-84-C-5089, "A New Radiographic Corrosion Inspection Capability." This program consisted of developing a dual-energy radiographic technique which could significantly enhance the corrosion detection and damage assessment capabilities of any radiometric system.

ARACOR acknowledges the generous assistance of Al Rogel, Nondestructive Inspection Manager, McClellan AFB, for his help in procuring the specimens of corroded parts studied during the course of this work.

ARACOR also acknowledges the support and feedback from our Contract Technical Monitor Mr. James Holloway and his AFWAL/MLLP colleague, Dr. Robert Crane.

Accession For	
NTIS	CRA&I <input checked="" type="checkbox"/>
DTIC	TAB <input type="checkbox"/>
Unannounced <input type="checkbox"/>	
Justification	
By	
Distribution /	
Availability Codes	
Dist	Avail and/or Special
A-1	



TABLE OF CONTENTS

	<u>Page</u>
1.0 INTRODUCTION.....	1
2.0 PROGRAM DESCRIPTION.....	1
2.1 Technical Rationale.....	2
2.2 Program Objectives.....	2
2.3 Technical Overview.....	3
2.4 Significance of the Dual-Energy Technique.....	5
3.0 SOFTWARE DEVELOPMENT.....	7
3.1 Selection of Parameters for Image Decomposition.....	7
3.2 Development of Calibration Procedures.....	8
3.3 Construction of Residual Images.....	10
3.4 Presentation of Simulation Results.....	11
4.0 EXPERIMENTAL RESULTS.....	21
4.1 Overview.....	21
4.2 Calibration Measurements.....	21
4.3 Test Object Scans.....	23
4.3.1 Dual-Energy Calibration Phantom.....	23
4.3.2 Aluminum--Saphire--Silicon Composite Phantom.....	23
4.3.3 Air Force-Supplied Antenna Panel.....	28
4.4 Discussion of Results.....	36
5.0 CONCLUSIONS AND RECOMMENDATIONS.....	37
5.1 Summary of Results.....	37
5.2 Recommendations.....	37
6.0 REFERENCES.....	38
APPENDIX Review of Dual-Energy Radiographic Principles.....	39

LIST OF FIGURES

<u>Figure</u>	<u>Caption</u>	<u>Page</u>
1	Simulated radiographs of calibration phantom.....	12
2	Compton-photoelectric separation of simulated calibration phantom radiographs.....	13
3	Graphite-titanium residual images of simulated calibration phantom radiographs.....	14
4	Simulated radiographs of sensitivity phantom.....	16
5	Compton-photoelectric separation of simulated sensitivity phantom radiographs.....	17
6	Corrosion-silicon residual images of simulated sensitivity phantom radiographs.....	18
7	Corrosion-silicon cancelled images of simulated sensitivity phantom radiographs.....	19
8	Photograph of calibration phantom.....	22
9	Radiographs of calibration phantom.....	24
10	Compton-photoelectric separation of calibration phantom radiographs.....	25
11	Graphite-titanium residual images of calibration phantom radiographs.....	26

LIST OF FIGURES (Continued)

<u>Figure</u>	<u>Caption</u>	<u>Page</u>
12	Photographs of aluminum stepwedge pair.....	27
13	Radiographs of aluminum stepwedges.....	29
14	Compton-photoelectric separation of aluminum stepwedge radiographs.....	30
15	Residuals after subtracting 6061 and 2024 aluminum alloys.....	31
16	Antenna panel.....	32
17	Dual energy digital radiography: Component radiographs.....	33
18	Compton-photoelectric separation of the antenna mount panel radiographs.....	34
19	Residuals of the antenna mount panel after subtracting the contribution of 7075 aluminum alloy.....	35

1.0 INTRODUCTION

This final report is submitted in fulfillment of the reporting requirements of AFWAL Contract No. F33615-84-C-5089, entitled "A New Radiographic Corrosion Inspection Capability." The report summarizes the results of an ARACOR SBIR Phase I effort conducted between 2 August 1984 and 8 April 1985 to evaluate the efficacy and sensitivity of a dual-energy radiographic method. A two-pronged research effort was developed and implemented, providing both simulated and actual dual-energy measurements. Based on the results of this work, it is concluded that a dual-energy technique can significantly enhance the corrosion detection and damage assessment capabilities of a digital radiographic system.

2.0 PROGRAM DESCRIPTION

Corrosion of equipment and material is a ubiquitous national problem. For the Armed Forces, preventing, detecting and repairing corrosion is a crucial part of their continuous struggle to keep military systems in full combat readiness. A recent study by the National Bureau of Standards, "Economic Effects of Metallic Corrosion in the United States," estimates corrosion-related problems cost the U.S. economy over \$70 billion annually. A similar figure has not been placed on corrosion losses within the Armed Forces, but it is certainly in the billions of dollars (1). In October 1980, the Joint Logistics Commander established a Joint Panel on Corrosion Prevention and Control with one of its specific mandates being to provide special emphasis on the development of new corrosion-sensitive NDI techniques with the potential to provide rapid, large-area inspections. Concurrently, a Joint Technical Coordinating Group on NDI was also established with the development of an effective corrosion inspection technique as one of their high priority objectives. As a result of these and other related efforts, a major workshop on the NDE of aircraft corrosion was held at Wright Aeronautical Laboratories, Dayton, Ohio, in May 1983. The dual-energy corrosion detection technique reported here emerged as a direct response to the proceedings of that workshop.

2.1 Technical Rationale

Detection of corrosion in real structures is complicated by the myriad of geometric configurations encountered in actual objects as well as by the fact that a significant amount of corrosion is either not immediately accessible to the inspector or is invisible to commonly used inspection techniques. Consequently, there is a general need for new inspection procedures and/or technologies which are more quantitative, more reliable, more reproducible, more rapid, more economical, and more forgiving than current methods. Real-time radiography has been identified as one of several technologies that offers significant promise of providing improved corrosion detection (1-4). Real-time systems have the potential to provide rapid, semi-quantitative inspection; and if the data are converted to digital format at some stage in the signal processing chain, various spatial- and temporal-mask subtraction techniques and a variety of enhancement routines could conceivably be used to provide an automatic corrosion detection and assessment capability. Yet, in spite of the potential advantages allegedly possessed by real time systems, they have not to date demonstrated a significantly better ability to detect corrosion in its early stages (when corrective actions can most efficiently be taken) than other competing modalities (2). ARACOR, which had been exploring dual-energy imaging methods as they apply to Computed Tomography for more than half a decade, recognized the possibility of significantly improving corrosion detection and assessment technology by applying dual-energy techniques to digital radiographic systems.

2.2 Program Objectives

The overall objective of the work reported here was to provide both simulated and actual demonstrations of dual-energy radiographic corrosion inspections. Software simulations are the most efficient means of rapidly ascertaining the general sensitivity of a new inspection method, and actual measurements of real components are the most definitive means of unequivocally establishing feasibility. As a result, a two-pronged research approach was conceptualized and implemented. The specific task-oriented objectives which were established and the rationale behind them can be enumerated as follows:

*** Perform Computer Simulations of Dual-Energy Corrosion Detection**

- . Most efficient method of determining the general sensitivity of the dual-energy technique.
- . Crucial for guiding actual experiments in the most fruitful and useful directions.
- . Required to provide an understanding of the computer architecture and software requirements that will be needed in an actual system.

*** Perform Actual Dual-Energy Measurements on a Suitable System**

- . Vital for corroborating the results of the computer simulations and for validating the parametric studies performed.
- . Necessary to provide unequivocal proof-of-principle demonstration of dual-energy methods.
- . Needed to uncover unanticipated problem areas so that a practical design of a dual-energy system can be more efficiently evolved.

The program effort was successful in accomplishing all of the goals set for it. The results of the software simulations are presented in the next section and the results of the actual measurements in Section 4. A summary of the conclusions and recommendations reached by this effort are given in Section 5.

2.3 Technical Overview

The term "dual-energy" is utilized in this context to indicate that as a standard part of the inspection procedure, radiographs are taken at two different effective energies and implicitly assumes that the radiographs are digital at some point in the processing so that they may be analyzed to provide additional information not otherwise available with conventional (single-energy) radiographic systems. The approach relies on the fact that in the energy range from a few keV to many MeV, all but a small number of minor effects are explainable in terms of just three photon-matter interactions -- photoelectric, Compton, and pair production; and that at energies below about 1 MeV, the Compton effect and the photoelectric effect dominate, while above several MeV, the Compton effect and pair production dominate[†]. Consequently, since no more

[†]An excellent introductory explanation of the physics of these processes can be found in (5) and a more advanced treatment in (6).

than two interactions need to be considered at one time to account for the attenuation of x-rays in matter when dealing with the physics of radiography, digital radiographs obtained at two different energies can be analyzed to obtain the individual contributions of the competing interactions to the total attenuation (7). Further, because the photoelectric and pair production effects are particularly sensitive to atomic number and the Compton effect is particularly sensitive to density, the effective atomic number and density of each point in a radiograph can be determined from projections taken at two different energies. In other words, detailed material properties can be extracted from dual-energy radiographs.

To get a sense of how this is accomplished, consider in somewhat more detail the physical basis for dual-energy digital radiography. Broadly speaking, the dual-energy technique relies upon two key approximations to the physics of the x-ray attenuation process. First, the assumption is made that the local mass absorption coefficient of the absorbing material, μ , can be adequately described in terms of only two attenuation mechanisms, μ_1 and μ_2 ; i.e.,

$$\mu(E, Z, A) \approx \mu_1(E, Z, A) + \mu_2(E, Z, A) \quad ,$$

where the full dependence of μ on the x-ray energy, E , and the local atomic number, Z , and the local mass number, A , of the material has been explicitly displayed. As stated above, describing μ as the sum of only two attenuation mechanisms is a good approximation for most radiographic situations. Second, the assumption is made that each attenuation coefficient can be adequately described as the product of two terms, one of which depends solely on the energy of the incident photon, the other of which depends strictly on the atomic number of the interacting matter, and neither of which carries an A dependence, i.e.,

$$\mu_i(E, Z, A) \approx \mu_i(E, Z) \approx \eta_i(E) \sigma_i(Z) \quad ,$$

where η represents the energy-dependent term and σ the Z -dependent term.

The dual-energy method leverages these approximations by recognizing that the description of the x-ray transport of a polychromatic beam through matter involves both an average over the energies in the incident flux and an integral along the ray path. Since the E and Z dependencies separate by construction, the line integral of μ along the beam path can be written as:

$$\int \mu(\hat{E}, Z) ds = \eta_1(\hat{E}) \int \sigma_1(Z) ds + \eta_2(\hat{E}) \int \sigma_2(Z) ds \quad ,$$

where ds is an element of length along the ray path of the beam and $\eta_1(\hat{E})$ and $\eta_2(\hat{E})$ are two constants that depend only on the effective energy, \hat{E} , of the fluence. The value of this fact is that η_1 and η_2 can be determined empirically by suitable calibration procedures and used to algebraically process two radiographs taken at different x-ray tube energies to extract a pair of new images, one that depends on $\int \sigma_1 ds$ and the other on $\int \sigma_2 ds$. Since σ_1 and σ_2 depend only on the material properties of the object of interest, they provide a method of determining the additional information about the material under examination.

One particularly powerful use of this technique is to "cancel" the predominant material in the image to improve the conspicuity of other materials that may be present. This is accomplished by performing a weighted subtraction of the σ_1 image from the σ_2 image, the relative proportions being selected so that $\sigma_1 = \sigma_2$ for the material the user wishes to eliminate. Since the magnitude of σ_1 and σ_2 vary systematically over the elements, in general only one element (or compound) at a time will be cancelled with this technique. Materials in the subtracted image with a higher atomic number will have a negative residual; those with a lower atomic number will have a positive residual (or vice versa, since the sign is arbitrary).

2.4 Significance of the Dual-Energy Technique

The power of the dual-energy technique is twofold: (1) it improves conspicuity by eliminating structural noise in the image; and (2) it allows the user to identify different materials in the object under examination. For instance, if an aircraft structure is composed largely of aluminum, then the

aluminum can be cancelled and the residual image studied. Only non-aluminum material would be present in the new image. Normally expected items, such as fasteners, gaskets, sealants, etc., would be readily recognized by the inspector; and any corrosion or other foreign matter, if it exists, would be visible as anomalous patches of unexpected material. Since non-aluminum items are generally well known and well specified; and since further, those areas most likely to corrode are presumably well defined, it should be a straightforward task to search for the presence of corrosion in susceptible components. This technique might also turn out to offer a rapid way to screen for missing components, such as critical washers or gaskets, since the conspicuity of small parts is greatly increased when more dominant materials are cancelled in a radiograph.

Further, dual-energy radiography can also be used in a more general way to identify materials. Starting with a normal image, the user can sequentially cancel one material after another while watching the residual image. When a particular structure or component suddenly disappears from the image, the operator can infer its material composition from the particular weighting used to achieve the cancellation. Although this may not be especially useful for identifying standard components where *a priori* information can more readily be used to identify material composition, it could on the other hand be very important in identifying foreign substances, differentiating contaminants, such as water from fuel, or in assessing the degree of corrosion present. The results of this work indicate that the effective atomic number of materials can be determined to better than three percent absolute error.

Thus, the dual-energy technique offers a powerful means of dealing with a large subset of corrosion detection problems. Foremost, it should significantly enhance or augment the corrosion detection and damage assessment capabilities of any real-time system. Furthermore, the improved sensitivity offered by dual-energy methods can be traded for an equivalent detectability at a much reduced dose level, an important consideration in close environments, such as on-board or in-situ inspections. In those areas where real-time radiography has already demonstrated, or is expected to demonstrate, an ability to produce useful inspections, the proposed technique will serve to improve the examination and to expand the range of valid applications. In those areas where real-time

radiography is at best marginal, dual-energy processing may make some otherwise impractical applications feasible. Either way, wherever real-time radiography finds an application in corrosion detection and prevention, dual-energy radiography will offer substantial improvements in detection sensitivity and damage assessment.

3.0 SOFTWARE DEVELOPMENT

The goal of the software development effort was to generate a set of algorithms which would allow digital radiographs of objects taken with two distinctly different bremsstrahlung spectra to be decomposed into images based on the competing attenuation mechanisms. A secondary goal was to perform detailed simulations to aid the development and provide an initial indication of the sensitivity of the technique.

The major tasks needed to achieve these goals were:

- * Selection of the parameterization to be used in the image decomposition;
- * Generation of an analytical representation of the calibration radiographs in terms of the selected parameters; and
- * Development of appropriate linear combinations of the parameter images to allow elemental cancellations.

The results of these subtasks are presented in the following subsections.

3.1 Selection of Parameters for Image Decomposition

The concept of elemental analysis by dual-energy radiography originated in the medical radiology community(8). The x-ray attenuation process in biological specimens at medical x-ray energies is dominated by Compton and photoelectric processes. Radiologists realized that since the Compton cross-section is nearly independent of x-ray energy (E) and atomic number (Z) while the photoelectric cross-section varies approximately as E^{-3} and Z^{-3} , it should be possible to distinguish the two attenuation processes from a pair of radiographs taken at different energies. However, early attempts did not produce particularly good results for two reasons: (1) initial models of the attenuation mechanism were not adequate to handle the presence of a weaker, but non-negligible, third

attenuation mechanism (i.e., Rayleigh, or coherent, scattering); and (2) the numerical methods of processing dual-energy data had not yet evolved to the point where results could be obtained efficiently. With the subsequent development of more efficient decomposition schemes and data processing techniques, medical dual-energy methods eventually evolved workable approaches. While these techniques produced adequate results with biological materials and relatively low-energy x-ray sources characteristic of medical systems, they were inadequate for industrial or military applications in which the predominant materials consist of higher-Z elements and radiometric densities require higher-energy sources to obtain adequate signal-to-noise levels.

For the range of materials of interest here, the absorption process is fed by three interactions, the Compton, the coherent (Rayleigh) and the photoelectric. The Z and E dependences of all three of these components are complex. The coherent cross-section is comparable to the Compton at low-energy and comparable to the photoelectric at high-energies. Just as it did for early medical attempts, the existence of a third interaction complicates matters significantly if not treated properly. The approach taken here was to model the attenuation process in terms of two fictitious cross sections which give a good fit to the mass absorption coefficients without trying to make a firm connection to the underlying details of the processes involved. The terminology Compton and photoelectric has been retained, however, because at high energies the one cross section is essentially the same as the Compton interaction while at low energies the other cross section is essentially the same as the photoelectric interaction.

3.2 Development of Calibration Procedures

Once a parameterization is selected, it is necessary to calibrate the parameterization by scanning an object of known composition and thickness. The approach used here was to describe the response of the system to the known calibration object in terms of the established model and thereby deduce the various free parameters in the model. Step wedges of titanium and graphite were selected for the calibration phantom and oriented perpendicular to each other. Graphite was chosen because the photoelectric contribution to its x-ray absorption is negligible above 40 keV. The choice of titanium was a compromise between the practical requirements for a material whose absorption is predominantly

photoelectric and whose mechanical properties permit it to be readily machined. Additionally, the two materials bracket the range of atomic numbers of interest and are also commercially available in highly homogeneous forms with excellent batch-to-batch uniformity.

Simulated high- and low-energy images of the calibration phantom were then generated. The simulation used a calculated bremsstrahlung spectrum, including the tungsten characteristic line radiation (k_α and k_β), based on the model of Reference 9. The spectrum was calculated at 1 keV intervals from 20 keV to the assumed tube voltage (250 keV for the low-energy spectrum, and 420 keV for the high-energy spectrum). The high energy spectrum was presumed to be filtered with 3 mm of brass to improve the contrast between the two images. The x-ray transmission was calculated for each energy bin and the results summed to give an integrated transmitted intensity for each graphite-titanium combination. The transmission calculations were performed using the mass absorption coefficients from Reference 10. Photon noise was also added to each measurement assuming Poisson statistics.

The assumption was then made that the Compton and photoelectric components of the low-energy and high-energy images of the calibration phantom, C and P respectively, could be represented to sufficient accuracy in the form:

$$\begin{aligned}C(x,y) &= f_1(H(x,y),L(x,y)) \\ P(x,y) &= f_2(H(x,y),L(x,y)),\end{aligned}$$

where f_1 and f_2 are polynomials in $H(x,y)$ and $L(x,y)$, the normalized high- and low-energy images, respectively. The advantage of this formulation is that if suitable functions, f_1 and f_2 , can be found, an especially rapid method of decomposing measurements into their component images can be employed. Two orthogonal functions, f_1 and f_2 , were chosen for their computational properties and a code was developed to extract the coefficients of the functions from the calibration data. The simulated calibration images were submitted to this calibration routine and the results were then evaluated by generating Compton and photoelectric images for a number of test cases. Some results are presented in Section 3.4.

3.3 Construction of Residual Images

The Compton and photoelectric images extracted from the simulated radiographs were further processed to demonstrate the cancellation of a particular material in an image. This was accomplished by taking, on a point-by-point basis, a linear combination of the component images. Thus, if $C(Z)$ is the Compton attenuation of a particular material and $C(Z) = k(Z) P(Z)$, where $P(Z)$ is the photoelectric attenuation and $k(Z)$ is a constant whose value is specific to the material to be cancelled, then the residual at each point in the image can be calculated as follows:

$$R = C(Z) - k(Z)P(Z).$$

With this prescription, the material of interest will vanish. If the object contains material with a lower atomic number than Z , a positive residual will result. If it contains material with a higher atomic number, the residual will be negative. This is illustrated in the examples given in Section 3.4.

A related approach is to form the best visual cancellation and then obtain an estimate of Z using parametric forms for $C(Z)$ and $P(Z)$. An analysis of the inherent errors in this approach reveal that the uncertainties are dominated by the uncertainty in the assumed value of A for a given Z . A review of the low- Z elements showed that the average value of Z/A for the naturally occurring stable elements is 0.474 ± 0.021 , for $2 \leq Z \leq 30$. There are several competing mechanisms which cause $\langle Z/A \rangle$ to fluctuate to this degree: (1) hydrogen has an anomalously high value of $Z/A = 1$, which drives $\langle Z/A \rangle$ for compounds with large hydrogen content strongly upwards; (2) low- Z compounds (i.e., $Z < 20$, which includes the corrosion-related compounds as well as the organics and many inorganics) are dominated by elements with $Z/A \sim 0.5$; and (3) higher- Z compounds (i.e., $20 < Z < 30$, which include the commonly occurring iron-series elements: iron, copper, and zinc) are dominated by elements for which $Z/A \sim 0.46$. Other sources of error include the accuracy of the parameterization ($\sim 1\%$) and the ability of the observer to empirically adjust the ratio of Compton and photoelectric images ($\sim 1\%$). When all sources of error are analyzed and quantitatively folded together, the ability of dual-energy radiography to identify an unknown material is found to be roughly three percent.

3.4 Presentation of Simulation Results

Simulated high-energy and low-energy images of a 16 step x 16 step calibration phantom were generated. These images are shown in Figure 1. The graphite thickness is constant horizontally with the thinnest step at the bottom of the image. The titanium thickness is constant vertically with the thinnest step at the left.

The coefficients of the calibration functions were extracted and used to generate Compton and photoelectric images of the step wedge phantom.[†] These images are shown in Figure 2. Because the photoelectric cross section of graphite is negligible, the photoelectric image is a good representation of the titanium component of the phantom. On the other hand, since the titanium has a significant Compton component in its absorption, the Compton image looks very similar to the high-energy image. However, if an appropriate fraction of the photoelectric image is subtracted point-by-point from the Compton image, the effect of the titanium can be removed from that image.

In the units used for the simulation, $C(Ti) = .6988 * P(Ti)$. By forming the following linear combination of images, a residual image which features the graphite is obtained, i.e.:

$$R(\text{graphite}) = C(x,y) - .6988 * P(x,y),$$

where R stands for the "residual" image. The result of the subtraction is shown in the left-hand portion of Figure 3. A similar procedure can be used to eliminate the graphite and feature the titanium. This is shown in the right-hand side of Figure 3. The quality of the subtractions is an indication of the validity of the approach.

[†]This is not a case of "data in, data out." The simulated images were generated from information in References 9 and 10 and, therefore, totally independent of the parameterization selected here on the basis of convenience, functionality, and performance.

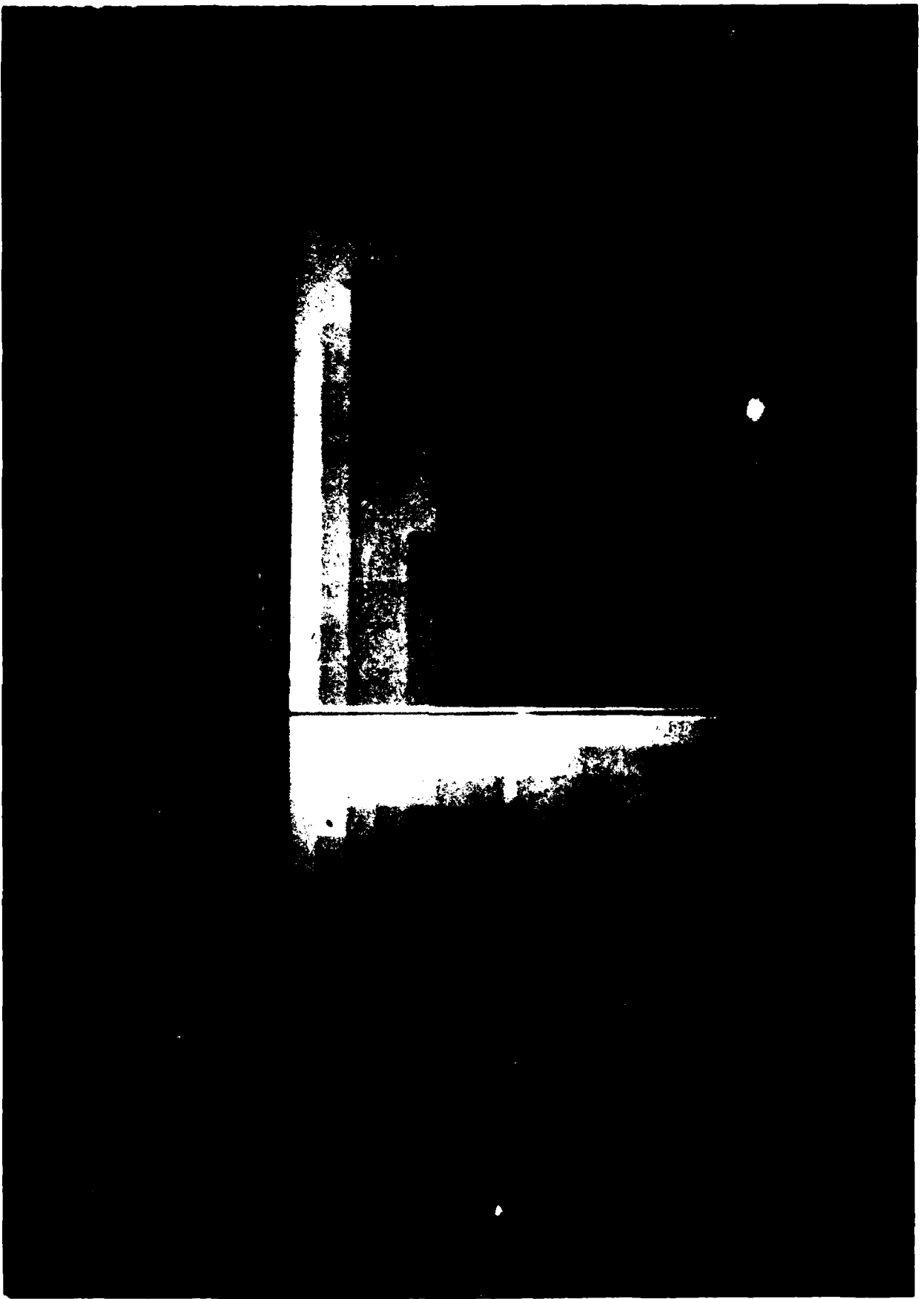


Figure 1. Simulated radiographs of calibration phantom.

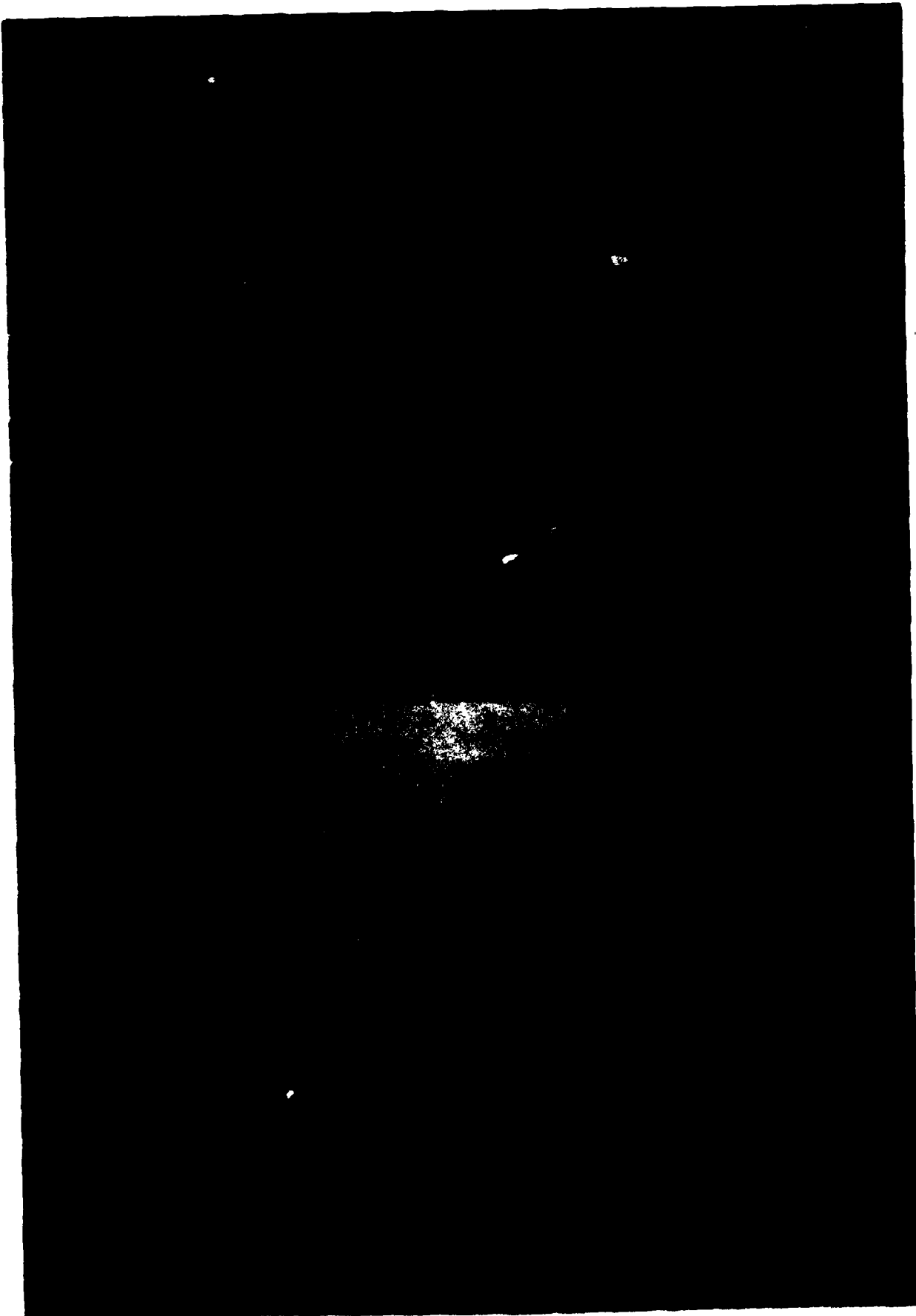


Figure 2. Compton-photoelectric separation of simulated calibration phantom radiographs.

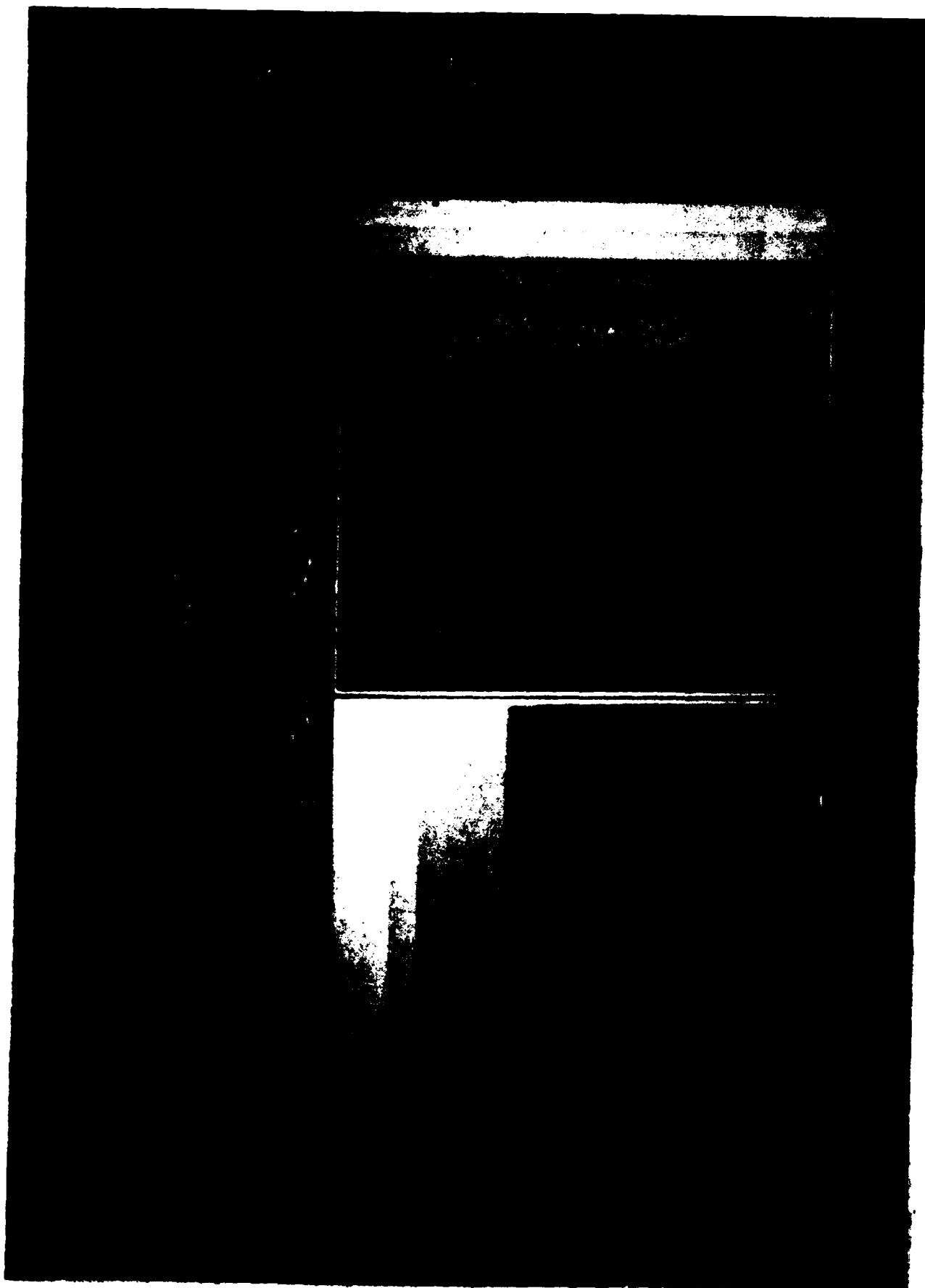


Figure 3. Graphite-titanium residual images of simulated calibration phantom radiographs

To test the sensitivity of the dual-energy imaging technique, another test was performed, this time using two new crossed step wedges, one aluminum and silicon and the other aluminum and aluminum-hydroxide. The images were combined in a single simulation by discarding every other aluminum step, producing a phantom whose lower half represents crossed steps of aluminum and aluminum hydroxide and the upper half crossed steps of aluminum and silicon. Figure 4 shows the simulated high- and low-energy radiographic images with noise added. Figure 5 shows the Compton and photoelectric images extracted from the high- and low-energy images. Because all three materials have a significant photoelectric component, these images differ little from the original radiographs. From a fit of the aluminum mass absorption coefficient, it can be shown that $C(Al) \approx 4.376 * P(Al)$. Thus the residual image formed by the point-by-point subtraction,

$$R = C(x,y) - 4.376 * P(x,y),$$

would be expected to cancel the aluminum in the image and obtain a positive residual if the object contains material with a lower Z than aluminum and a negative residual if the object contains material with a higher Z than aluminum. The resultant positive and negative residual images are shown in Figure 6. With the aluminum cancelled, the silicon and aluminum hydroxide step wedges are clearly resolved.

Next, an initial measure of the sensitivity of the technique was obtained by empirically adjusting the relative proportions of the Compton and photoelectric images required to cancel first the silicon step wedge and then the aluminum hydroxide one (see Figure 7). The ratios corresponding to the best visual cancellation were then inverted to obtain an estimate of Z.

The empirically adjusted ratio for a silicon cancellation was 3.503 and for aluminum hydroxide 7.548. These ratios produced a calculated value of $Z = 14.2 \pm 0.2$ for silicon and 11.4 ± 0.2 for aluminum hydroxide. Both agree within the expected error with the accepted value of Z (or in the latter case, the effective value of Z).

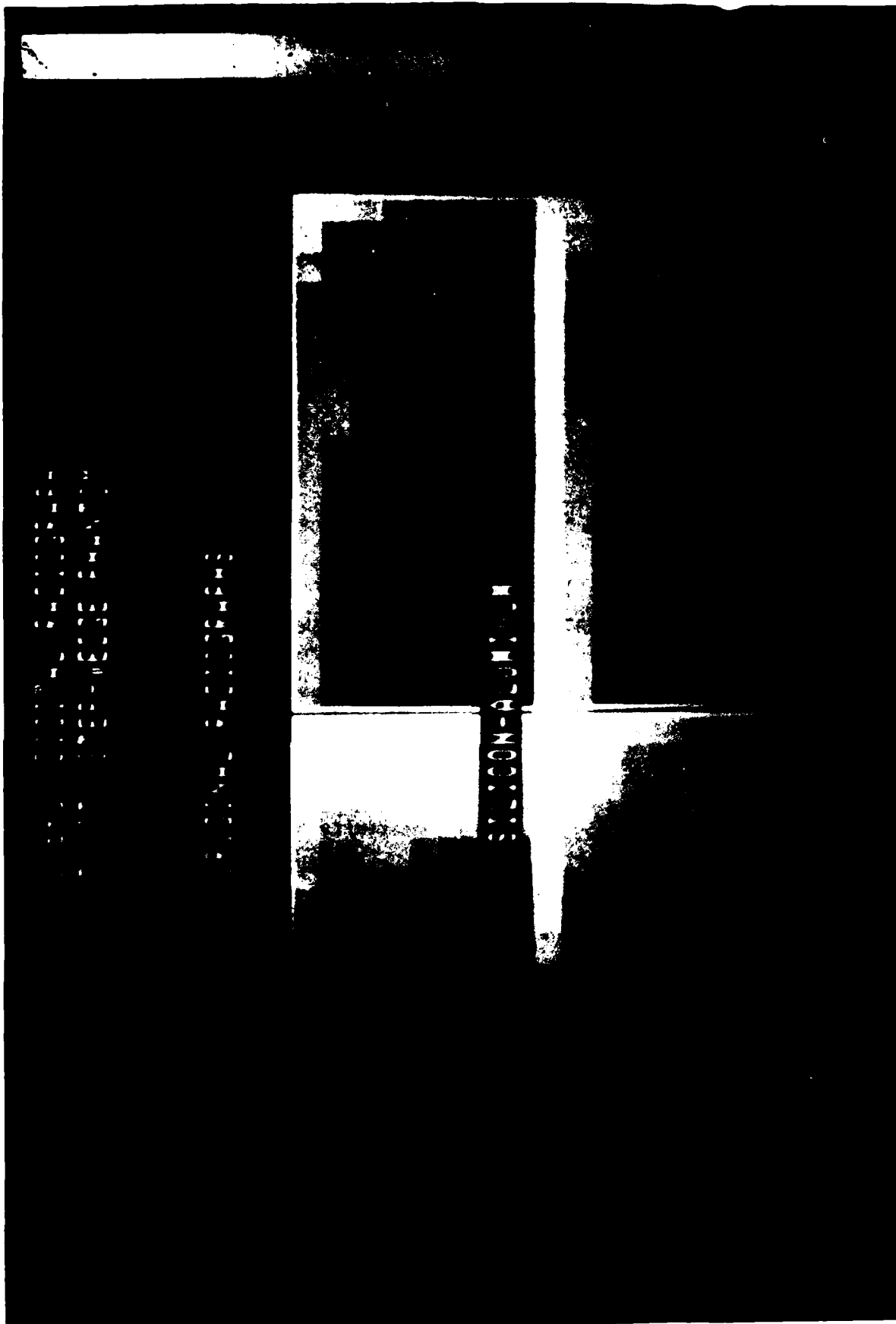


Figure 4. Simulated radiographs of sensitivity phanto

LOW-ENERGY DIGITAL RADIOGRAPHY
SENSITIVITY STEP-WEDGE PHANTOM

COMPTON-PHOTOELECTRIC SEPARATION



Figure 5. Compton-photoelectric separation of simulated sensitivity phantom radiographs.

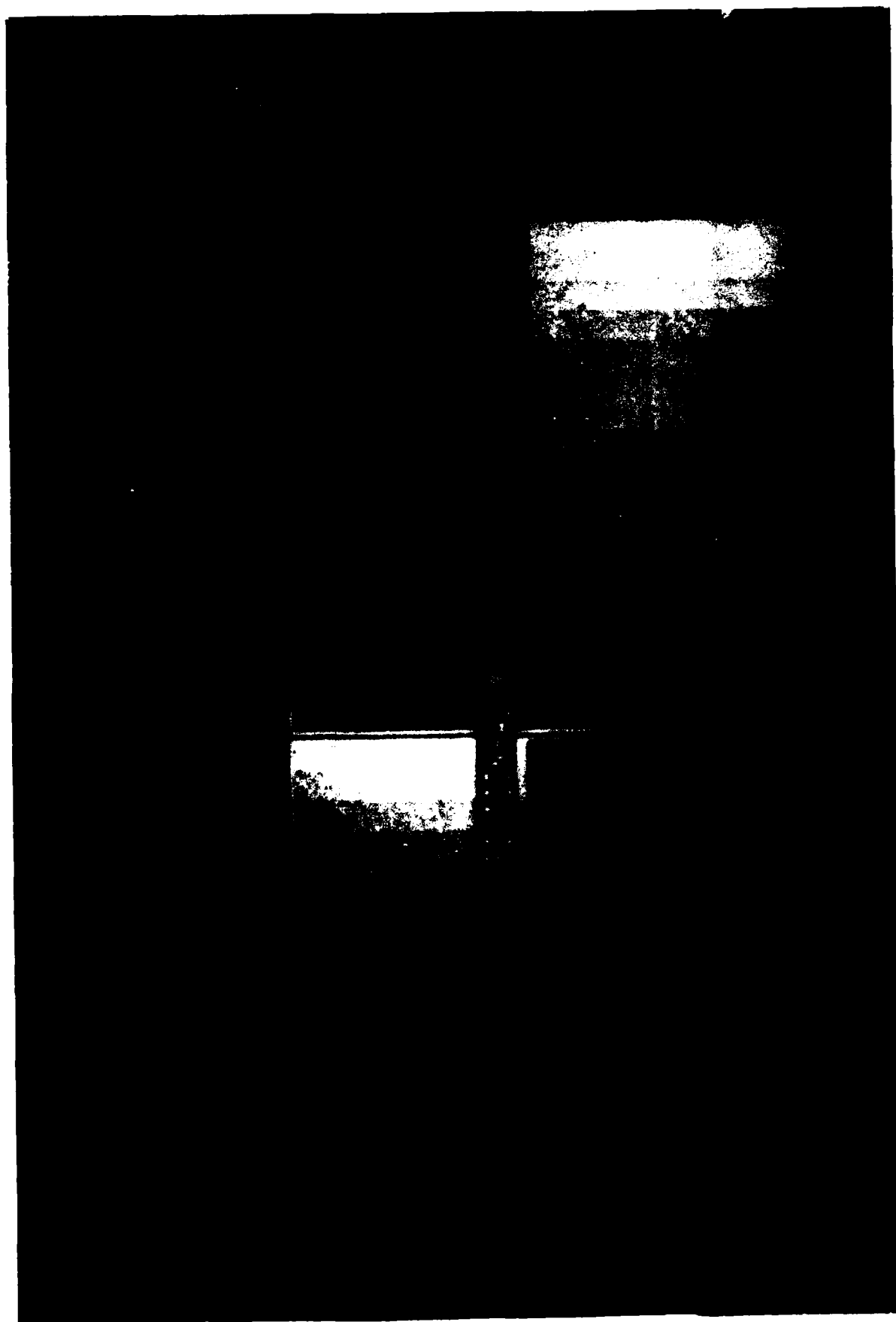


Figure 6. Corrosion-silicon residual images of simulated sensitivity phantom radiographs.



Figure 7. Corrosion-silicon cancelled images of simulated sensitivity phantom radiographs.

This appears to be a good estimate of the typical sensitivity of the technique in a practical situation when no other information is utilized. On the other hand, if additional *á priori* information is available, further improvement is possible. One approach is to use an iterative calculation to obtain a better estimate of Z . To do this, a higher value of $\langle Z/A \rangle$ is used when the initial estimate of Z is less than 20[†] and a lower value if Z is greater than 20. As an example, when the value of $Z \approx 14.2$ was obtained, a more reasonable value of $\langle Z/A \rangle = 0.5$ was used to recompute a value of Z on the grounds that most elements with a Z on the order of 14 tend to have a value of Z/A nearer 0.5. The once-iterated value of Z obtained in this way was 14.0, the correct value for silicon. The same calculation for the aluminum hydroxide gave a revised estimate of Z -effective of 11.2, which compares acceptably with the "true" value of 10.8.

[†]Roughly speaking, $\langle Z/A \rangle$ equals the mean value of 0.474 given above for values of Z near 20. (See Section 3.3).

4.1 Overview

To test the procedures developed with the aid of simulated data on real images, access to a digital radiographic system was arranged. The Air Force Advanced Computed Tomography System Number One (AF/ACTS-I) was selected on the basis of its proximity and availability to ARACOR, our familiarity with its data acquisition system, and the unit's ability to produce high quality dual-energy radiographic images. The dual-energy methods developed here, however, are quite general and the demonstration could have been conducted on any real-time, or near-real-time, system capable of producing digital radiographs at different effective energies.

Several typical specimens of corroded parts were provided for study by Al Rogel, Nondestructive Inspection Manager, McClellan AFB. The item selected for the most detailed testing was an aluminum antenna panel with subsurface corrosion within stress-induced delaminations. To complement this object, ARACOR also developed a special test phantom for analyzing sensitivity. Results of these studies are presented in this section.

4.2 Calibration Measurements

The calibration phantom consisted of crossed step wedges, one of graphite and the other of titanium, each comprised of 16 steps. The titanium steps were 10.2-cm long by 0.625-cm wide while the graphite steps were 10.80-cm long by 0.597-cm wide. Thus there was a segment of each graphite step which was not overlaid with titanium, and a segment of each titanium step which was not overlaid with graphite. This construction resulted in a total of 17×17 distinct titanium-graphite thickness combinations or elements (see Figure 8).

The calibration measurements were conducted by highly oversampling each element of the calibration phantom at both energies. The low-energy scans were performed at 250 kV with no additional filtration; the high-energy ones at 420 kV with 3-mm brass additional filtration. The data for each "element" of

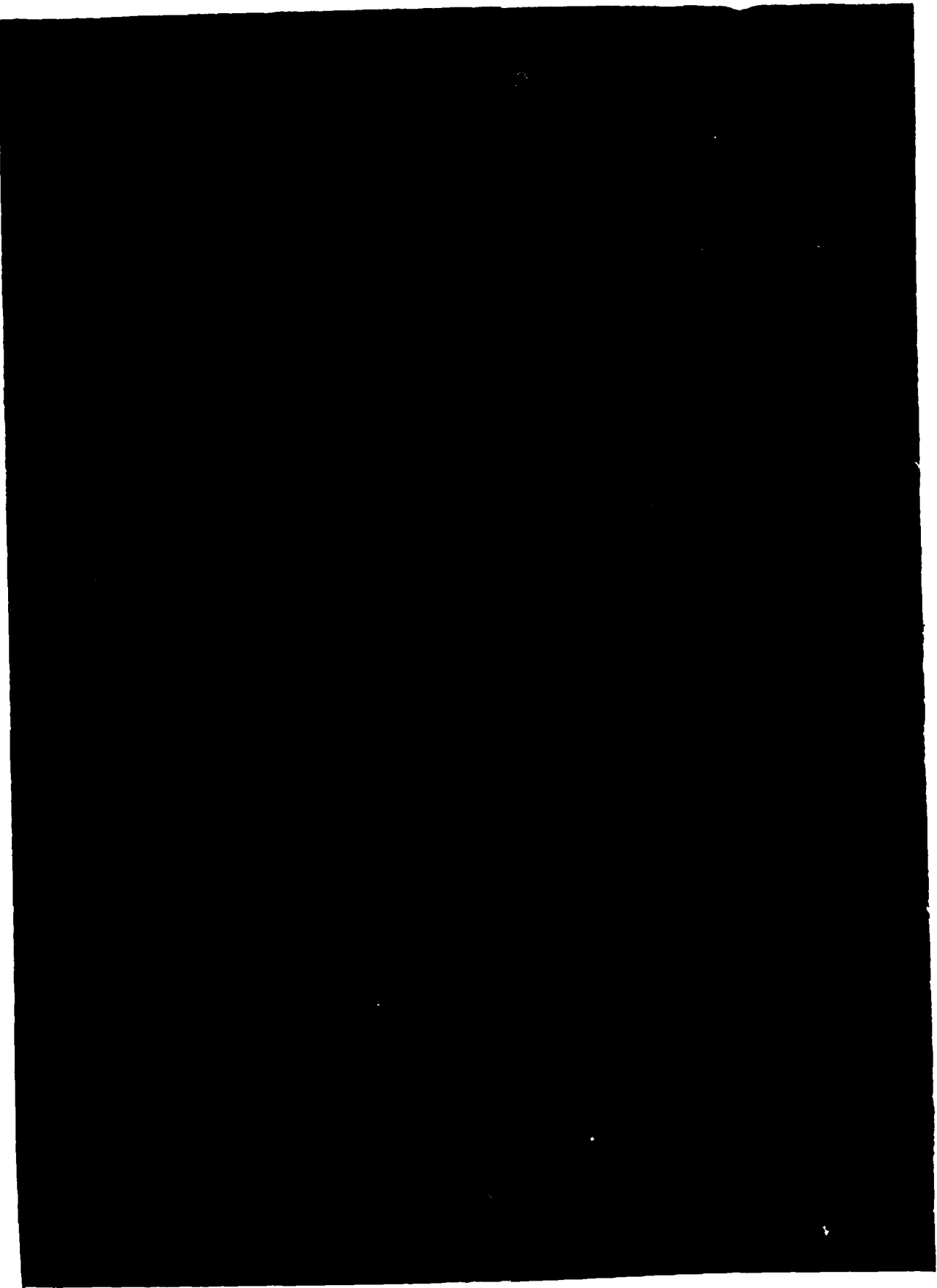


Figure 8. Photograph of calibration phantom.

the phantom were then averaged before being input to the calibration routine. Because of finite beam size and the fact that the beam traversed the step wedges at a different angle for each detector array element, it was necessary to develop an algorithm to select only the data points for which the entire beam passed through the full thickness of each graphite-titanium element and to apply a correction for the apparent thickness due to the different angles of incidence. The data set passed to the calibration program consisted of an average of a minimum of 500 data points for the thickest steps and up to a maximum of 1100 data points for the thinnest steps. The standard deviations of the mean values of the data were typically less than one percent, and the fits obtained from the calibration code were found to be excellent.

4.3 Test Object Scans

Radiographic image data were obtained for a number of objects. Three examples are shown here.

4.3.1 Dual-Energy Calibration Phantom. Figure 9 shows high- and low-energy digital radiographs of the calibration phantom taken with the tube operated at 250 and 420 kV. Figure 10 shows the extracted Compton and photoelectric images. As with the simulated images, the titanium step wedge is well defined in the photoelectric image, whereas the Compton image is not materially different from the original images. Figure 11 shows the result of subtracting 0.7 times the photoelectric image from the Compton image. As in the simulations, the graphite step wedge is now well developed in the resulting image.

4.3.2 Aluminum--Sapphire--Silicon Composite Phantom. A pair of aluminum step wedges used in some preliminary dual energy tests were also scanned. These were placed side-by-side with pieces of 0.010" thick silicon and 0.015" thick sapphire taped to the flat back surfaces. A photograph is shown in Figure 12. This object was intended to test the ability of the technique to distinguish materials that differ only slightly in effective atomic number. As will be seen, this phantom, due to an inadvertent error on the part of the machinist who made them, provided the most dramatic demonstration of Z-sensitivity of all of the objects studied.

DUAL ENERGY DIGITAL RADIOGRAPHY

COMPONENT RADIOGRAPHS



250 kV

Figure 9. Radiographs of calibration phantom.

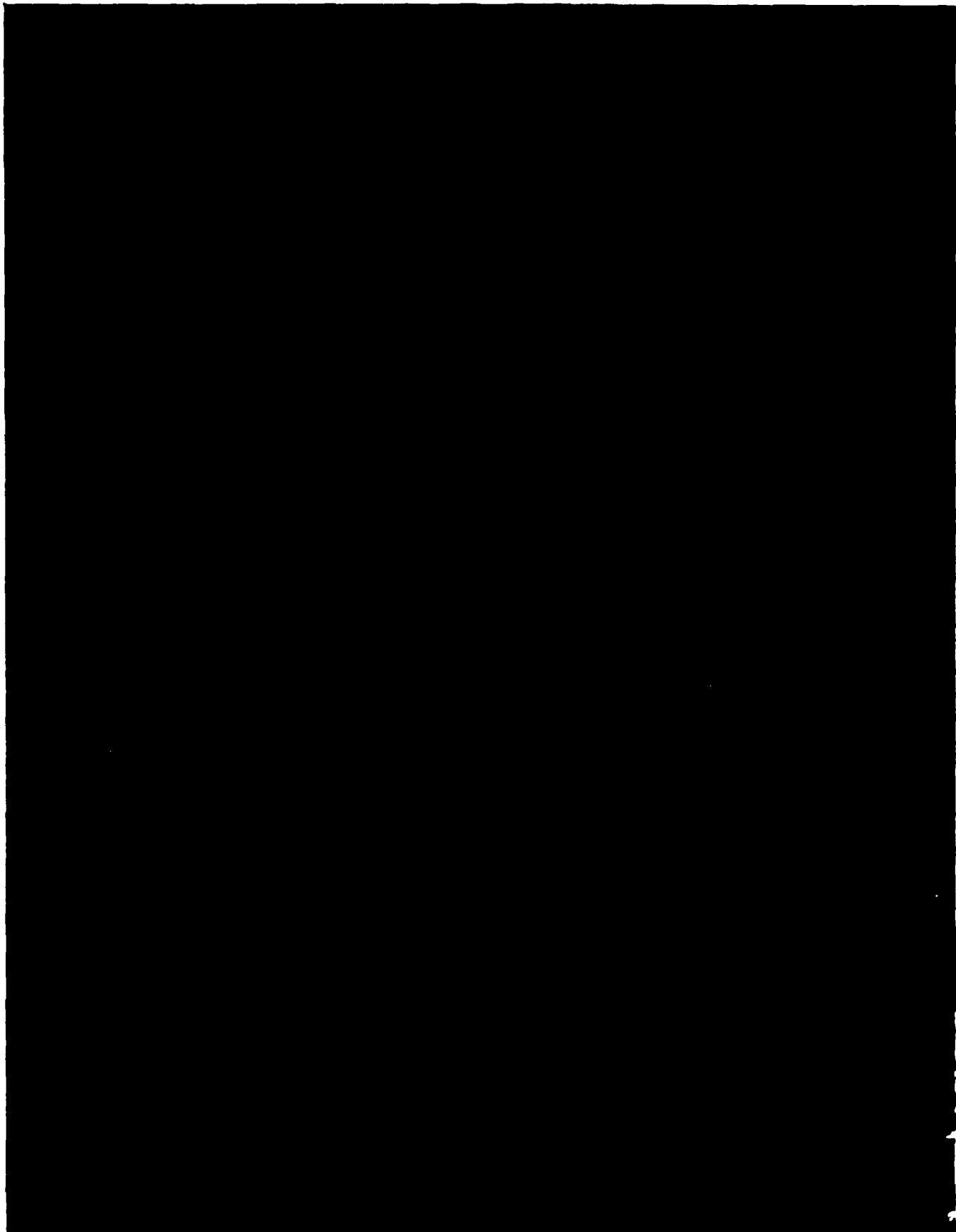


Figure 10. Compton-photoelectric separation of calibration phantom radiographs.

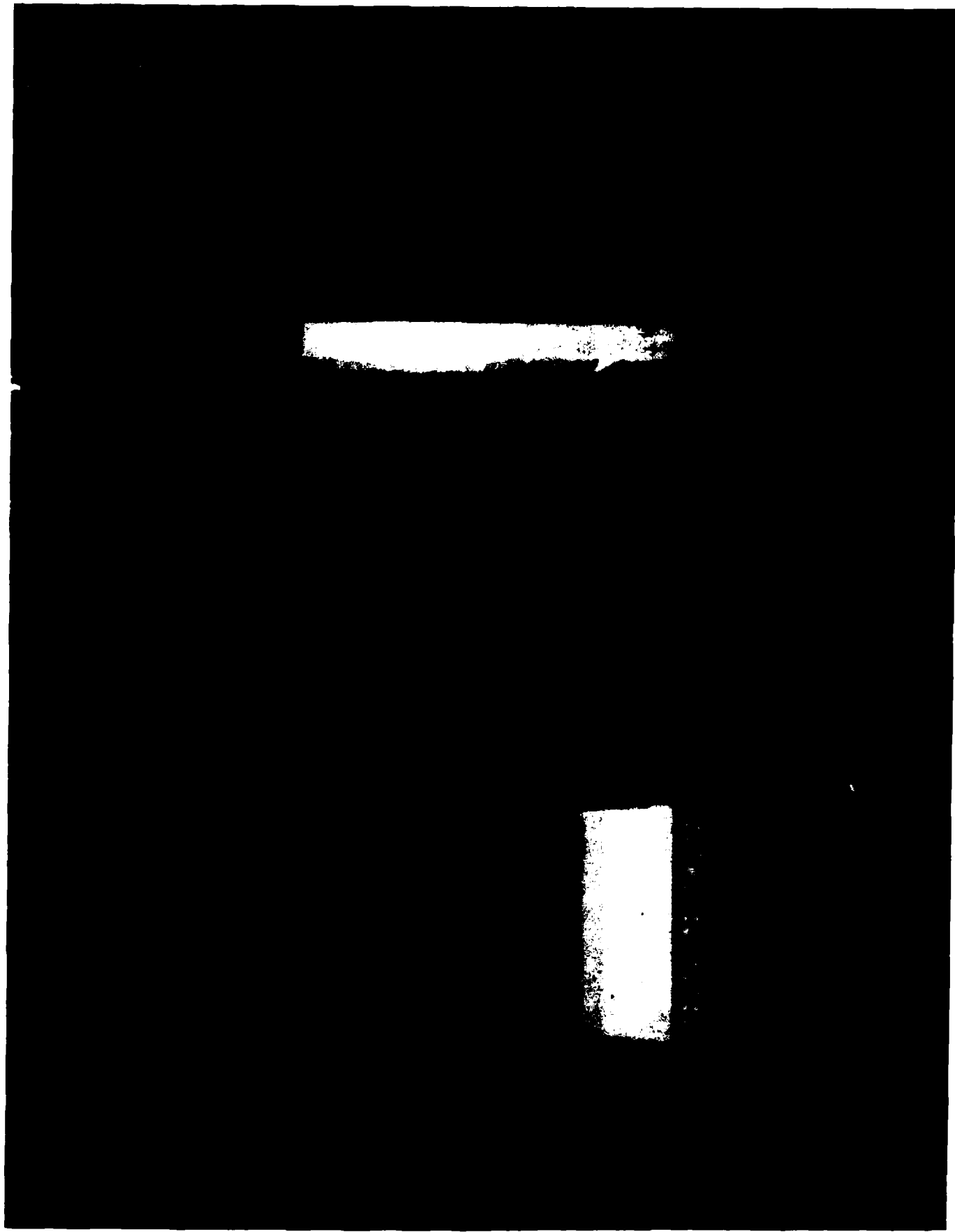


Figure 11. Graphite-titanium residual images of calibration phantom radiographs.



Figure 12. Photographs of aluminum stepwedge pair.

The radiographic scan data is shown in Figure 13. The five steps on the left are one piece of aluminum, and the four steps on the right are a second piece of aluminum. Figure 14 shows extracted Compton and photoelectric images. A serious anomaly is immediately evident. Since the bulk of the material is aluminum, the relative contrast of the two aluminum pieces should be similar. This is clearly not the case. The aluminum steps on the right clearly have a larger photoelectric attenuation than the aluminum steps on the left. The Compton-to-photoelectric ratio for the left stairs of aluminum is 3.7; for the right ones, it is 2.35. For pure aluminum, the expected ratio is 4.4. In an effort to interpret these results, the expected Compton-photoelectric ratio for several common aluminum alloys was calculated. On this basis, the alloy on the right was tentatively identified as either 7075 or 2024. The alloy on the left was tentatively identified as 6061. A spectroscopic analysis determined that the alloys were 2024 and 6061, respectively.

Figure 15 shows images with the 6061 subtracted and with the 2024 subtracted. The left-hand image shows negative residuals, i.e., regions with higher apparent atomic number (Z). Since the effective Z of 6061 is nearly the same as that of silicon and higher than that of sapphire, we do not expect to see any of the wafer fragments in this image. The right-hand image shows positive residuals (regions of lower Z than Al-2024). Here both the sapphire and silicon fragments can be distinguished.

4.3.3 Air Force-Supplied Antenna Panel. Figure 16 is a photograph of a corroded antenna mount panel supplied by the Air Force as a test sample. The dual-energy scans of this sample are shown in Figure 17. The extracted Compton and photoelectric images are shown in Figure 18. The panel was assumed to be made of the aluminum aircraft alloy 7075. The nominal composition of 7075 gives an effective Z of 15.3. Figure 19 shows the residuals with the Photoelectric image subtracted from the Compton image for effective Z 's of 15.3 (the predicted value) and 15.4 (the value which gave the best enhancement of the corrosion). The corrosion is visible as the badly-eroded region at the left center of either image. The major portion of this corrosion is beneath the surface of the panel within what appears to be stress-induced delaminations. The small but definite difference between the two images gives a qualitative sense for both the accuracy and the sensitivity with which the effective Z of a material can be determined.

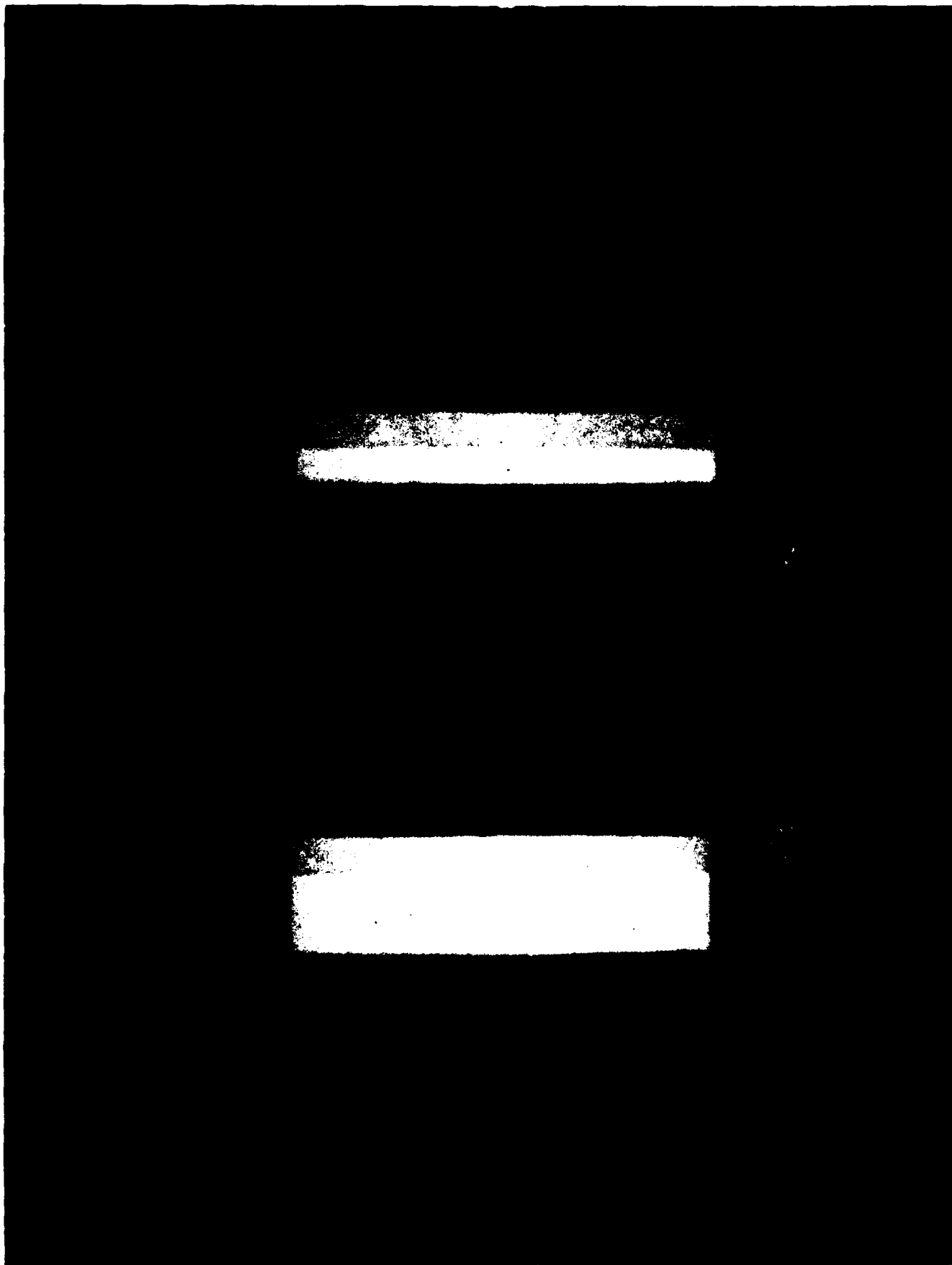


Figure 13. Radiographs of aluminum stepwedges.

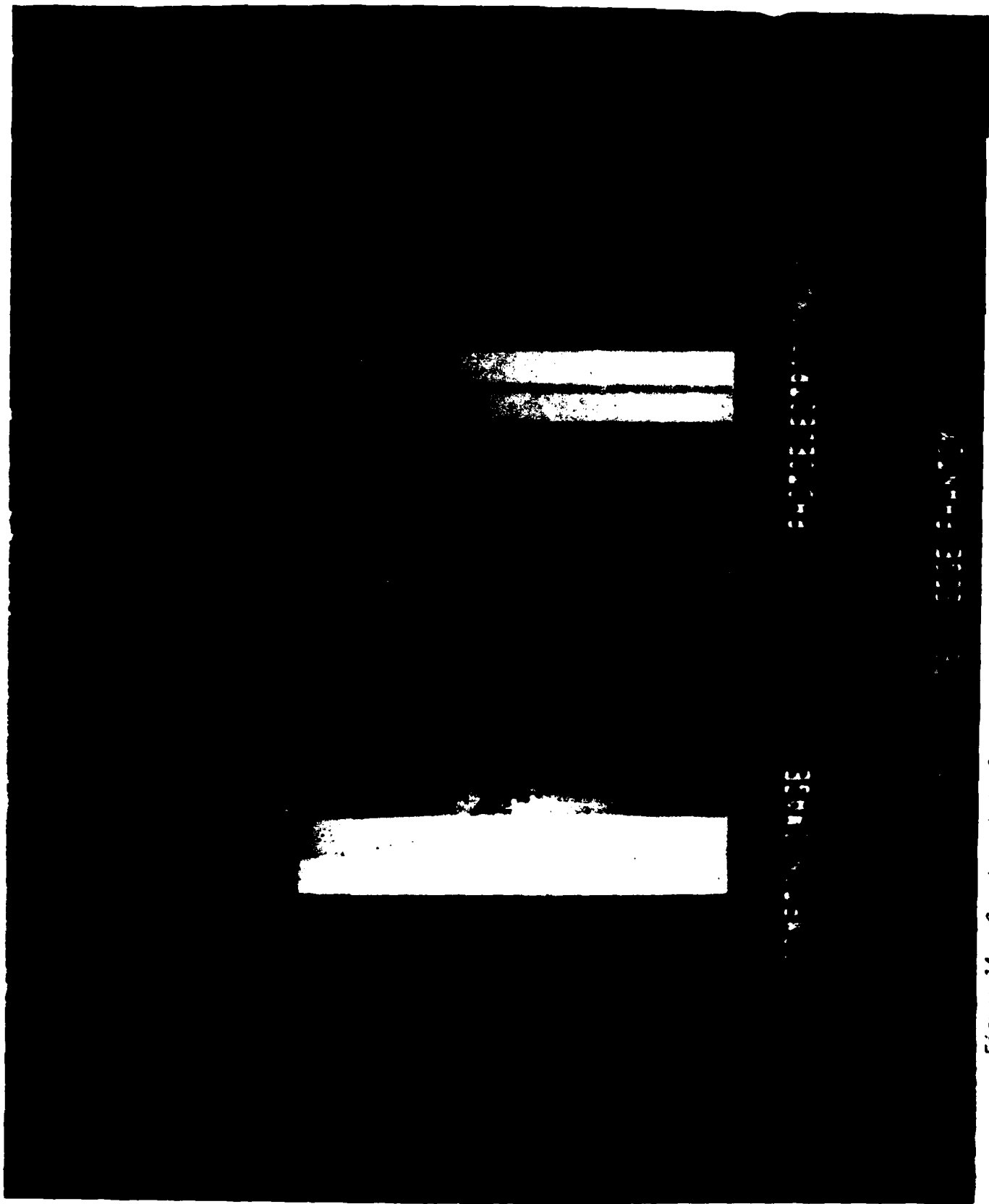


Figure 14. Compton-photoelectric separation of aluminum stepwedge radiographs.

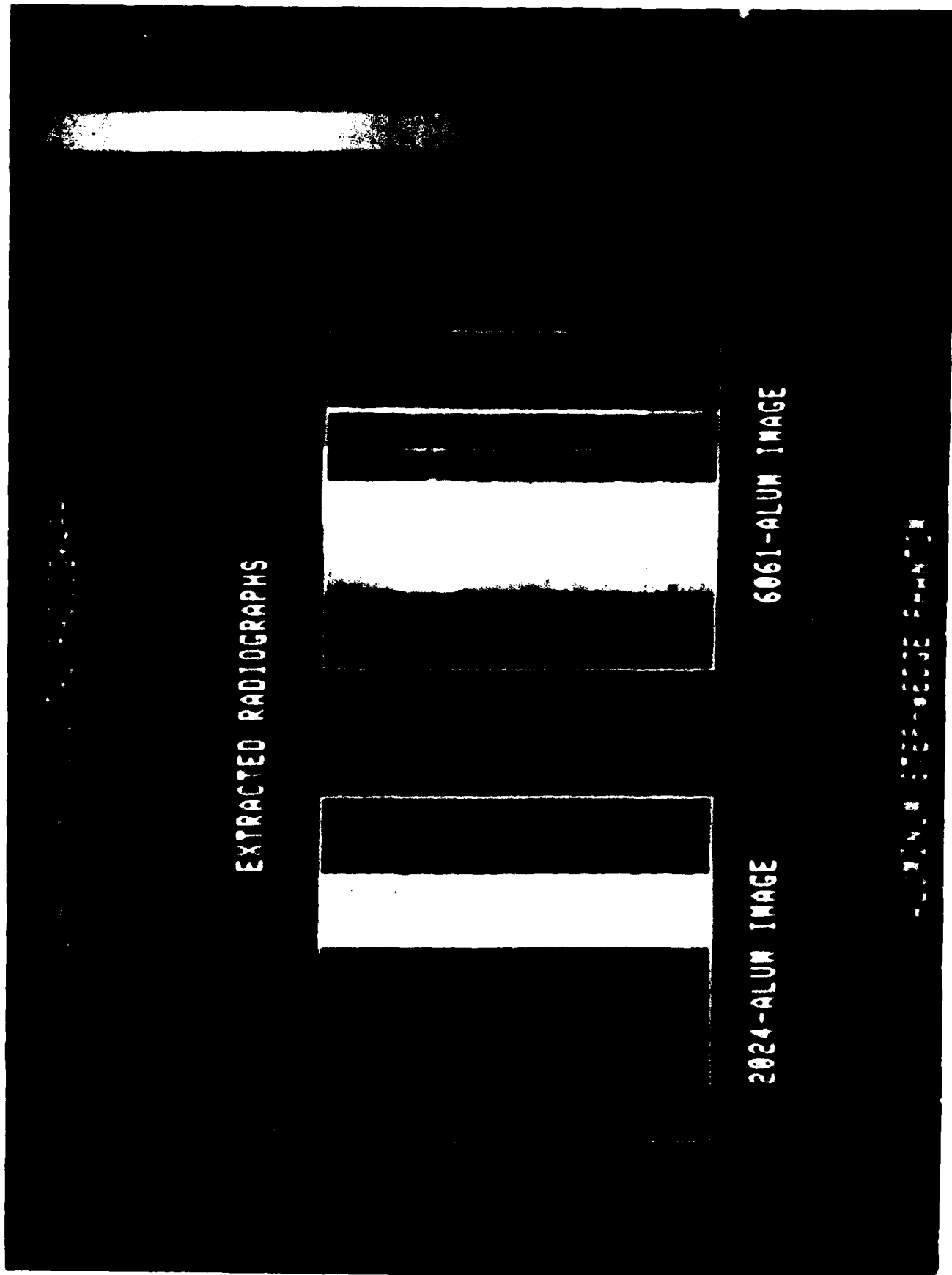


Figure 15. Residuals after subtracting 6061 and 2024 aluminum alloys.

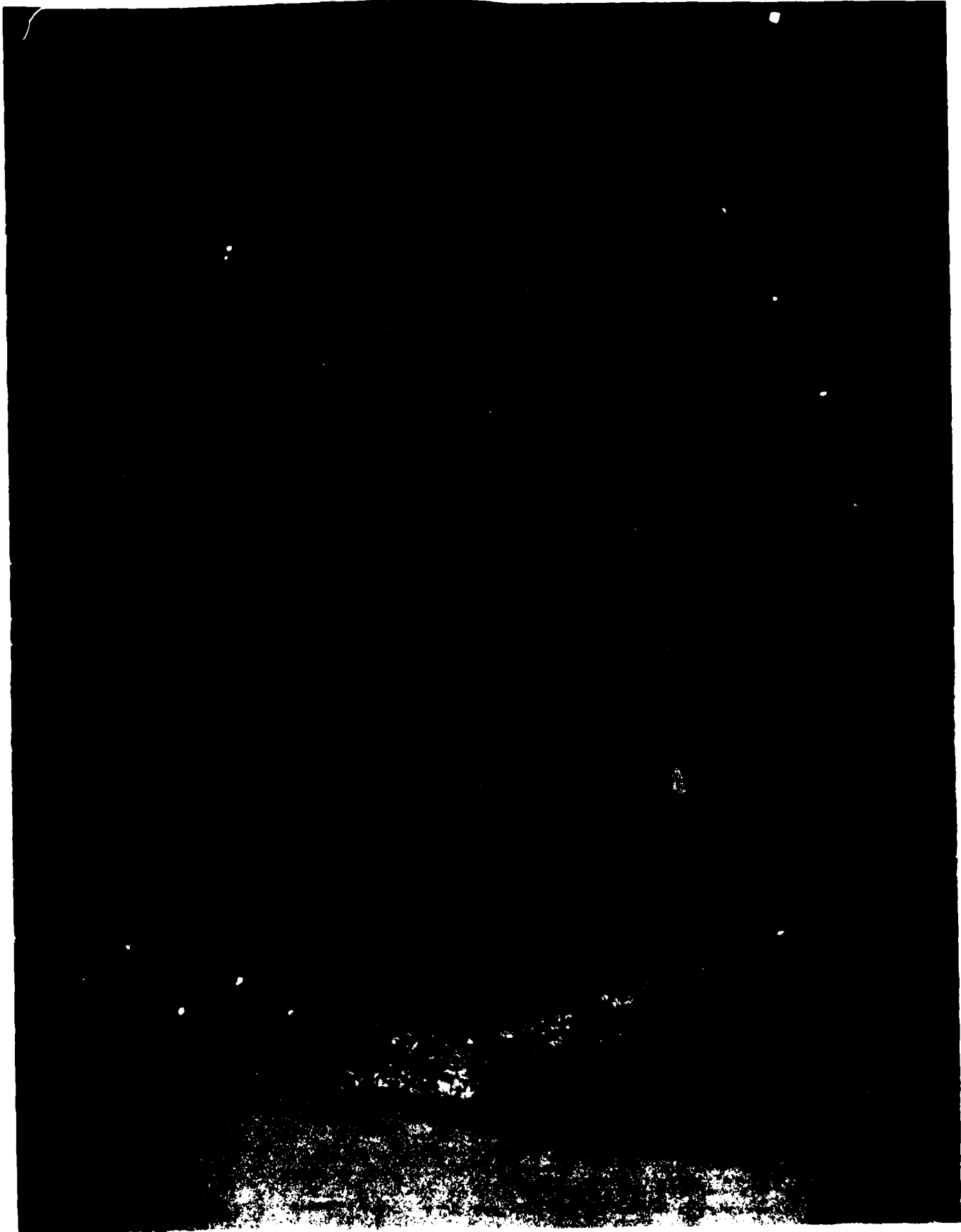


Figure 16. Antenna panel.

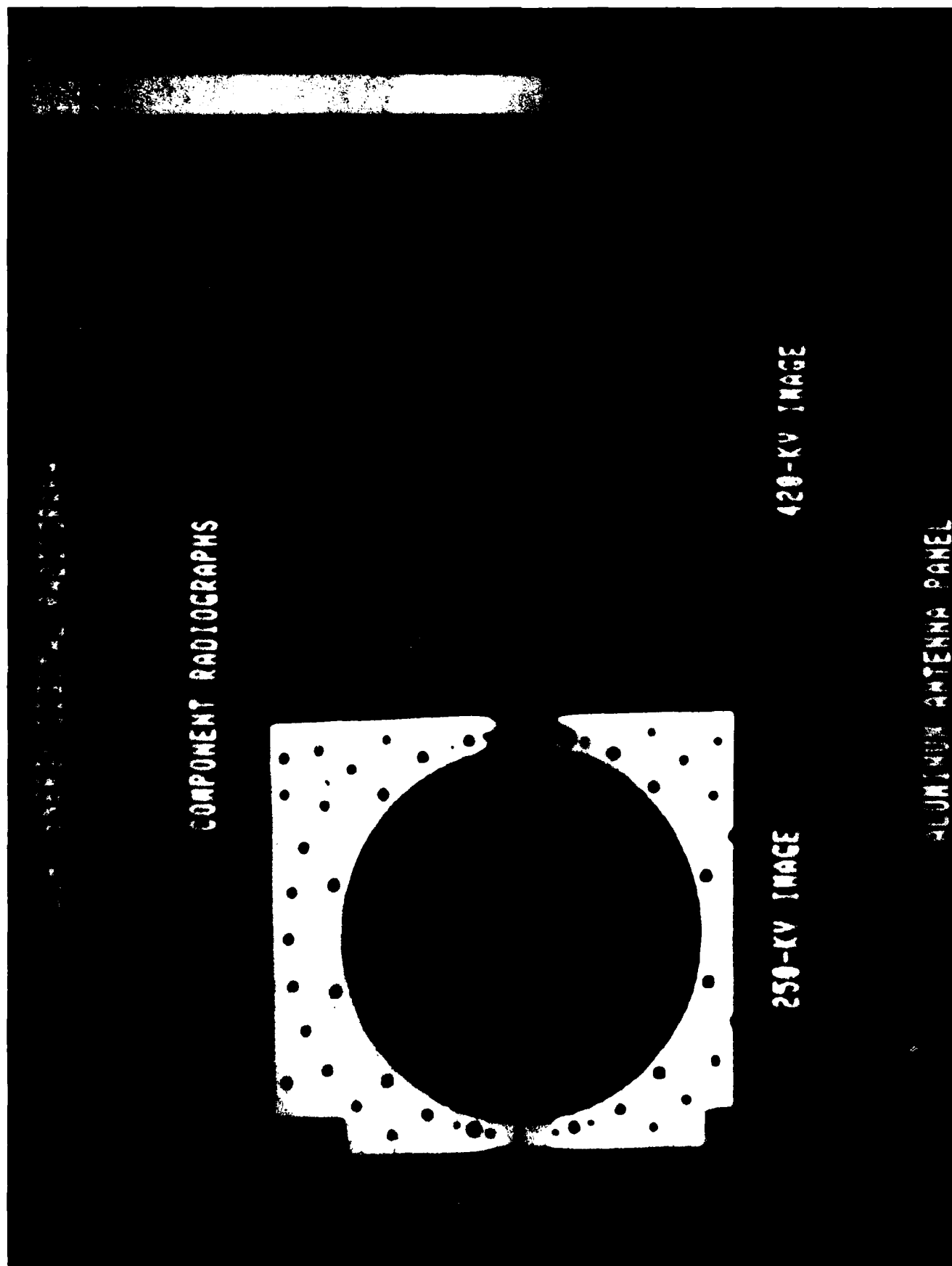


Figure 17. Dual energy digital radiography: Component radiographs.

DUAL ENERGY DIGITAL RADIOGRAPHY

SEPARATED RADIOGRAPHS

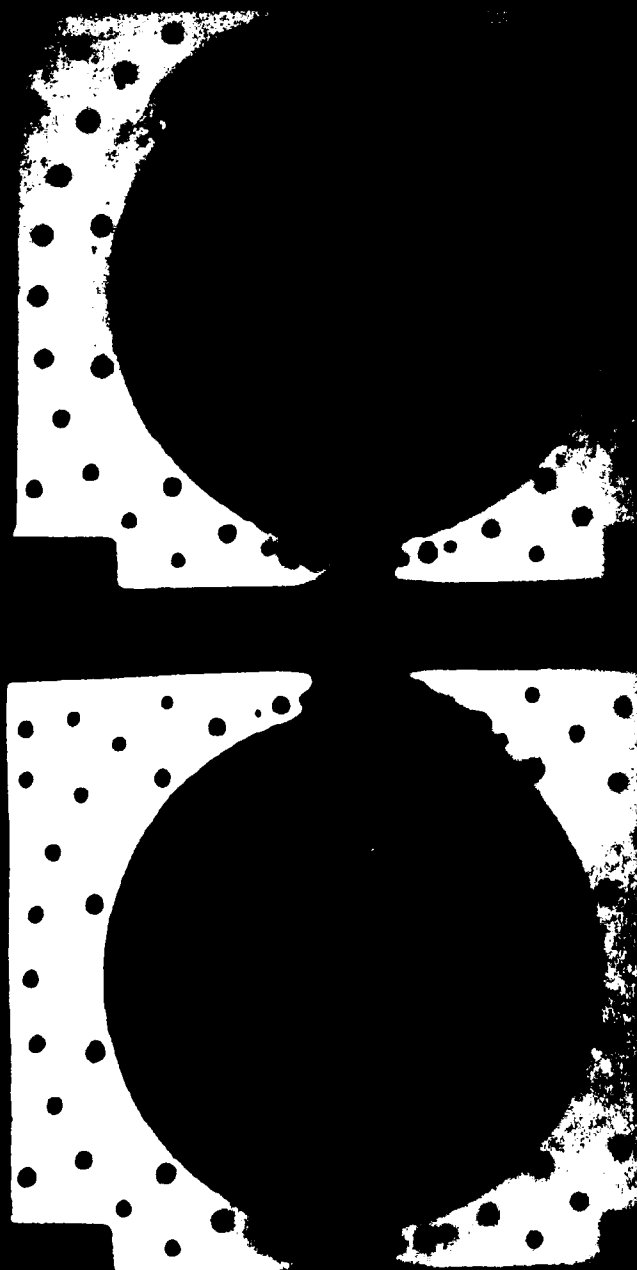


Figure 18. Compton-photoelectric separation of the antenna mount panel radiographs.

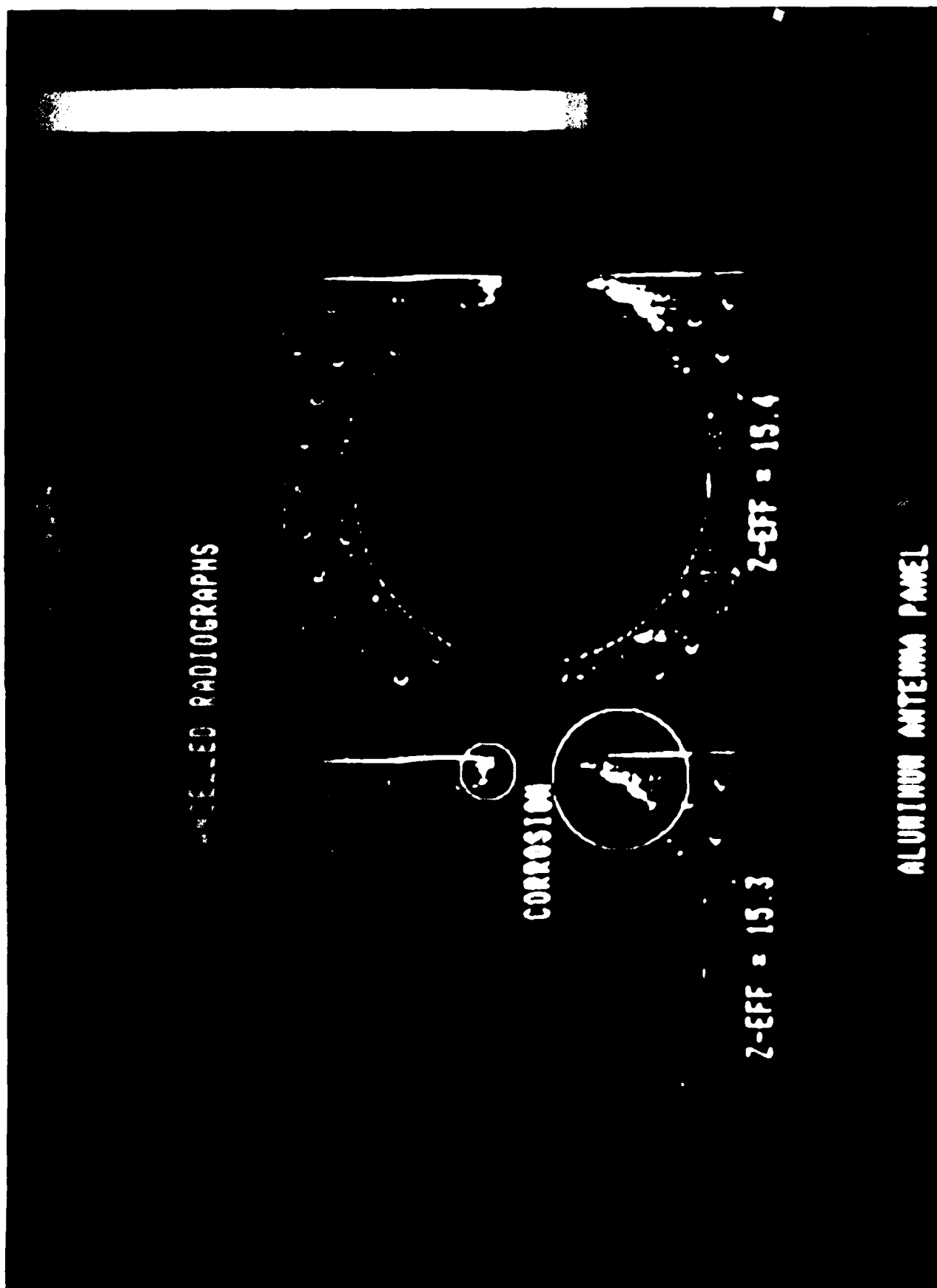


Figure 19. Residuals of the antenna mount panel after subtracting contribution of 7075 aluminum alloy.

Also visible are some small holes around the inner periphery of the panel which have been plugged with an aluminum alloy which has significantly lower Z than the panel material.

4.4 Discussion of Results

The principle of material identification and bulk material subtraction in dual energy images has been convincingly demonstrated in these experiments. While it is, perhaps, not surprising that the Compton-to-photoelectric ratio which was used in the generation of the fit coefficients should produce a good separation of the titanium from the graphite in the images of the calibration phantom, it is very encouraging that this ratio can also be calculated quite accurately for other materials, such as the various aluminum alloys studied here.

Several correctable deficiencies are apparent in the images obtained. First, improvements in both the signal-to-noise ratio and the signal stability would be desirable. Second, the thinnest calibration phantom steps should be thinner if relatively thin specimens (such as the antenna panel) are to be optimally imaged. Third, the x-ray beam could have profitted from additional filtration at 250 keV. And, lastly, a difference in the x-ray spot size or position manifests itself in the bright borders that consistently appear at discontinuities in the image. Methods exist which can reduce or eliminate this problem.

5.0 CONCLUSIONS AND RECOMMENDATIONS

5.1 Summary of Results

We have successfully developed the techniques and generated the computer algorithms for extracting elemental information from dual-energy radiographs. We have demonstrated both by simulation and with real data that the technique can be used to distinguish materials of different atomic number and can enhance the conspicuity of minor components of an object by cancelling the dominant structure in the object. In particular, the technique can be used to greatly enhance the visibility of corroded material in an image by eliminating structural noise associated with more dominant material in the component of interest. Further, the technique is of general validity and can in principle be adapted to any radiographic system capable of generating digital images at different effective energies. Thus, it is the general conclusion of this study, that dual-energy radiography can significantly enhance the performance of real-time systems and deserves consideration as an adjunct to future and existing radiographic units.

5.2 Recommendations

Because the technique depends on obtaining accurate absolute values of x-ray transmission, the requirements on the data acquisition electronics are quite stringent but well within the current state of the art. Development of a linear detector array specially tailored for dual-energy scans would improve the results obtained here, perhaps significantly. Thus, the development of a linear array tailored to and suitable for pursuing further, more quantitative, evaluations of dual-energy radiography is strongly urged.

6.0 REFERENCES

1. Proceedings of the AFWAL/ML Workshop on Non-destructive Evaluation of Aircraft Corrosion," Dayton, Ohio 24-25 May 1983.
2. Packer, M. E. "Applications of Image Processing to the Detection of Corrosion by Radiography," Materials Report 109. Aeronautical Research Laboratories, Defense Science and Technology Organization, Department of Defence, Australia (1979).
3. Wilcox, M. T. and D. L. Hanson. "Real-Time Fluoroscopic Image System for Honeycomb Bond Structures," Materials Evaluation, August (1981) 844.
4. Kulkarni, S. B. "NDT Catches Up With Composite Technology," Machine Design, April (1983) 38.
5. Johns, H. E. and J. R. Cunningham. Physics of Radiology," Third Edition, Thomas (1980).
6. Evans, R. D. The Atomic Nucleus, McGraw-Hill (1972).
7. Alvarez, R. E. "Extraction of Energy-Dependent Information in Radiography," Ph.D. Thesis, Dept. Elec. Engr., Stanford University (1976).
8. "SPIE Proceedings of Conference on Digital Radiography," Stanford University Medical Center, California, 14-16 September (1981).
9. Birch, R. and M. Marshall. "Computation of Bremsstrahlung X-ray Spectra," Phys. Med. Biol., 24, 505-517, (1979).
10. McMaster, W. H., et al. "Compilation of X-ray Cross Sections," UCRL-50174, Section 2, R-1, (1969).

APPENDIX

REVIEW OF DUAL-ENERGY DIGITAL RADIOGRAPHIC PRINCIPLES

There are four basic types of photon interactions with matter: (1) interactions with atomic electrons; (2) interactions with nucleons; (3) interactions with the electric field surrounding nuclei or electrons; and (4) interactions with the meson field surrounding nucleons. The effect of any of these interactions can result in: (1) complete absorption of the incident photon; (2) elastic scattering of the incident photon; or (3) inelastic scattering of the incident photon. Thus, in theory, there are 12 different processes by which electromagnetic radiation can be absorbed or scattered by matter. In the energy range from a few keV to many MeV, it turns out all but a small number of minor effects are explainable in terms of just three of the twelve processes. These are the photoelectric effect, the Compton effect, and the pair production effect. An excellent introductory explanation of the physics of these processes can be found in (7) and a more advanced treatment in (8).

An important additional simplification occurs when the energy of interest is well below or well above 1 MeV. In both instances, the physics of the attenuation process simplifies still further, being dominated by just two of the three principle attenuation mechanisms. In the former case, the attenuation process can be described to an excellent approximation as the result of photoelectric and Compton interactions; in the latter case, as the result of Compton and pair production interactions. Of the two cases, only the low-energy situation has been well studied, and it is this case which is presented here.

As a result, we write for present purposes the linear x-ray attenuation coefficient as the sum of two terms, one representing attenuation due to photoelectric interactions, designated τ , and one representing attenuation due to Compton interactions, designated σ . That is,

$$\mu(E,S) = \tau(E,S) + \sigma(E,S) . \quad (1)$$

The individual interactions in Eqn. 1 can be rewritten as follows:

$$\tau(E,S) = N(S) \cdot \tau_a(E,S) \quad (2a)$$

and

$$\sigma(E,S) = N(S) \cdot \sigma_a(E,S) \quad , \quad (2b)$$

where $N(S)$ is the number of atoms per unit volume at locality S and τ_a and σ_a are the atomic interaction cross sections. $N(S)$ equals the product of Avogadro's number, N_0 , and the ratio of the local material density, $\rho(S)$, and the local mass number, $A(S)$. That is,

$$N(S) = \frac{N_0 \rho(S)}{A(S)} \quad . \quad (3)$$

The atomic interaction cross sections can also be rewritten to explicitly exhibit their dependencies on the local atomic number, $Z(S)$, and the energy of the incident photon, E . From references (7,8), the atomic cross sections can be represented with sufficient accuracy for present purposes as:

$$\tau_a(E,S) = K_T Z^4(S) f_T(E) \quad (4a)$$

and

$$\sigma_a(E,S) = K_\sigma Z(S) f_\sigma(E) \quad , \quad (4b)$$

where f_T and f_σ carry the energy dependencies of the interactions and K_T and K_σ are dimension-carrying constants independent of photon energy or material composition. Thus,

$$\tau(E,S) = \frac{N_0 \rho(S)}{A(S)} \cdot K_T Z^4(S) f_T(E) \quad (5a)$$

and

$$\sigma(E,S) = \frac{N_0 \rho(S)}{A(S)} \cdot K_\sigma Z(S) f_\sigma(E) \quad (5b)$$

The crucial feature of Eqn. 5 is the fact that the spatial and energy dependencies (S and E) separate. That is, Eqn. 5 can be rewritten as

$$\tau(E,S) = a_T(S) f_T(E) \quad (6a)$$

and

$$\sigma(E,S) = a_O(S) f_O(E) \quad , \quad (6b)$$

where a_T and a_O carry strictly the spatial dependencies shown in Eqn. 6 and f_T and f_O carry strictly the energy dependencies. With the aid of Eqn. 5, Eqn. 6 can also be expressed in the following manner:

$$\tau(E,S) \propto \rho(S) Z^3(S) \cdot f_T(E) \quad (6c)$$

and

$$\sigma(E,S) \propto \rho(S) \cdot f_O(E) \quad , \quad (6d)$$

where Eqn. 6c and 6d makes note of the fact that the ratio Z/A is approximately constant over the entire periodic table (except for hydrogen). Consequently, the photoelectric attenuation is roughly proportional to ρZ^3 and the Compton attenuation to ρ .

The essential result of this discussion can now be derived. In radiography, the observed x-ray intensity, $I(E)$, can be related to the incident intensity, $I_0(E)$, by the well-known law of radiation physics:

$$I(E) = I_0(E) \exp \left[- \int_I \mu(E,S) dS \right] \quad , \quad (7)$$

where $\int_I \mu(E,S) dS$ represents the line integral of the linear attenuation coefficient of the object, $\mu(E,S)$, along the ray path I defined by the particular projection of the object being taken. For a monochromatic flux, the line integral of $\mu(E,S)$ along the given ray path can be readily extracted by forming the negative natural logarithm of the ratio of $I(E)/I_0(E)$,

$$L(E) = - \ln(I/I_0) = \int_I \mu(E,S) dS \quad . \quad (8)$$

When the incident spectrum is polychromatic, the prescription given by Eqn. 8 for extracting the value of $\int \mu dS$ is still valid provided E is interpreted as the effective energy of the x-ray beam. Since the effective energy varies as the ray path through the object changes, the calibration procedure becomes more complicated, the overall validity of the method is not affected.

Utilizing the results of Eqns. 1 and 6, Eqn. 8 can be rewritten in the following more convenient form:

$$L(E) = \int_{\Gamma} \mu(E, S) dS = \int_{\Gamma} (\tau(E, S) + \sigma(E, S)) dS \quad (9a)$$

$$= f_{\tau}(E) \int_{\Gamma} a_{\alpha}(S) dS + f_{\sigma}(E) \int_{\Gamma} a_{\sigma}(S) dS \quad (9b)$$

$$= c_1 L^{\tau} + c_2 L^{\sigma}, \quad (9c)$$

where in Eqn. 9, $f_{\tau}(E)$ and $f_{\sigma}(E)$ have been replaced by constants, c_1 and c_2 , to emphasize that they depend solely on the effective energy of the incident radiation and L^{τ} and L^{σ} are line integrals along the same ray path and depend solely on the material properties of the object.

The implication is as startling as it is simple: if scans are performed at two different effective energies, E and E' , then L^{τ} and L^{σ} can be extracted separately, point-by-point, by solving the following pair of simultaneous equations:

$$L(E) = c_1 L^{\tau} + c_2 L^{\sigma} \quad (10a)$$

and

$$L(E') = c_1' L^{\tau} + c_2' L^{\sigma}. \quad (10b)$$

If the data sets from two identical x-ray projections[†], $\{L(E)\}$ and $\{L(E')\}$, were noiseless, then any two different effective energies would suffice; but of course, in any non-mathematical context they cannot be. This implies that some care must be taken to engineer (to the extent possible) a situation that will produce the greatest degree of linear independence between the above equations. Stated another way, the solution to Eqn. 10 will depend on the statistical accuracy of the measurements, $L(E)$ and $L(E')$, and the nature of the determinant of the coefficients on the right hand side of the equation. It is assumed that the measurements can be engineered so that $c_1 c_2' - c_1' c_2$ is well conditioned and non-zero, and that exposures are sufficient to obtain well-behaved data sets. In practice, there is sufficient flexibility that these are not severe constraints. Thus, in the following development, it will be supposed that the two effective energies are well separated and that the measurements are statistically accurate, two demands which are, at least intuitively if not quantitatively, well defined.

[†]The notation adopted here uses brackets to indicate a collection of ordered points which constitute an image.

Under these conditions, Eqn. 10 can be solved straight-forwardly, point-by-point, over the whole image with the result:

$$\{L(E)\}, \{L(E')\} \Rightarrow \{L^T\}, \{L^\sigma\} \quad . \quad (11)$$

In words, Eqn. 11 states that the two new images, $\{L^T\}$ and $\{L^\sigma\}$, can be generated from the dual-energy images, $\{L(E)\}$ and $\{L(E')\}$, to obtain radiographs proportional to the material-dependent portions of the projected object. It also states further that since $a_{T\alpha\rho}(S)Z^3(S)$ and $a_{\sigma\alpha\rho}(S)$, the so-called dual-energy images provide a powerful method of sampling the density and atomic number within an object of interest. It is this potential access to two fundamental material attributes that make dual-energy radiography such an attractive technique for corrosion detection.

To see how this would work in practice, consider the following important extension of the above derivation. Eqn. 11 states that a high- and a low-energy images, $\{L\}$ and $\{L'\}$, can be decoupled to produce two, more fundamental images, one proportional to the density of the projected material and one proportional to the product of the density and the cube of the atomic number of the projected material. However, and this is the key point, these two derived images, $\{L^T\}$ and $\{L^\sigma\}$, can in turn be manipulated to produce an almost endless series of new images which, though less physical in nature, are nevertheless considerably more practical from the standpoint of corrosion detection.

The basic procedure is to form linear combinations of $\{L^T\}$ and $\{L^\sigma\}$ in such a way as to achieve some useful advantage. Since this is done point-by-point, the brackets can be dropped for convenience without loss of generality in the following discussion. First, define a general linear combination of the photoelectric and the Compton image as follows:

$$R = kL^T + k'L^\sigma \quad , \quad (12)$$

where k and k' are constants and R stands for a point in the resultant (or residual) image. It can be seen immediately by comparing Eqn. 12 with Eqn. 9c that if k is taken equal to c_1 and k' to c_2 , R just becomes one of the original images. It may appear as though we have just reversed our earlier efforts; but

properly viewed, this result is far from trivial. It implies that by taking physically meaningful values for k and k' , we can produce radiographs at any effective energy we wish from our two dual-energy images. This might be very important in scanning for low-contrast detail in some applications.

On the other hand, other more general linear combination can also be formed. Perhaps the most powerful of these approaches for corrosion detection is the one that seeks to cancel a designated material. Imagine for concreteness that an object consists predominantly of aluminum. In this case, the line integrals shown in Eqn. 9 can be written as a term integrated over the projected aluminum material and a term integrated over whatever residual material is also present. Carrying the separation forward, Eqn. 12 can be rewritten as:

$$R = k(L^T(AI) + L^T(res)) + k'(L^\sigma(AI) + L^\sigma(res)) \quad (13a)$$

$$= [kL^T(AI) + k'L^\sigma(AI)] + [kL^T(res) + k'L^\sigma(res)] \quad , \quad (13b)$$

where $L(AI)$ and $L(res)$ stand for the appropriate integrals over the projected amounts of aluminum and residual materials, respectively. By examination, it can be seen that by taking:

$$\frac{k'}{k} = - \frac{L^T(AI)}{L^\sigma(AI)} \quad , \quad (14)$$

the aluminum contribution to any point R can be made to vanish. Thus, by performing the subtraction on a point-by-point basis over the whole image, the residual (non-aluminum) material in the object, R , can be viewed with all aluminum detail "magically" cancelled.

This is obviously a very significant and powerful result. For one thing, it implies that dual-energy techniques can be used to remove dominant structure in an image and reveal low-contrast detail that might not otherwise be observed due to structural noise. For another, it suggests that this method can also be used to help identify foreign materials within an object. To see this more clearly, consider Eqn. 14 again. Since L^T is proportional to ρZ^3 and L^σ is proportional to ρ , it follows that

$$\frac{k'}{k} \propto Z^3 \quad (15)$$

In general, one would not expect to have to identify the internal detail in an object. That would be known a priori from assembly drawings. However, if a foreign substance or unexpected object were to appear in a radiograph, the operator could adjust k and k' (perhaps automatically with a joystick or trackball) until the item of interest exactly disappears from the residual image. The atomic number of the item could then be inferred from the ratio of k and k' using Eqn. 15. It is conceivable that this procedure could prove useful for assessing corrosion progression since, in some circumstances, the severity of the corrosion present might be proportional to the relative amounts of oxide, salt, and/or hydride formed. That is, dynamics of the situation might be such that shifts in the average atomic number of the corroded material could be correlated with the degree of progression of the damage.

END

FILMED

6-86

DTIC